EXPERIMENTAL AND NUMERICAL INVESTIGATION OF MECHANICAL EFFECT OF EXTERNALLY WEAK LAYERS IN THICK HYBRID COMPOSITES

By
SAHER GUL

Submitted to the Faculty of Engineering and Natural Sciences
in partial fulfillment of
the requirements for the degree of
Master of Science

Sabanci University
December 2019

EXPERIMENTAL AND NUMERICAL INVESTIGATION OF MECHANICAL EFFECT OF EXTERNALLY WEAK LAYERS IN THICK HYBRID COMPOSITES

APPROVED BY:

Assoc. Prof. Dr. Burcu Saner Okan (Thesis Supervisor) .....

Asst. Prof. Dr. Adnan Kefal (Thesis Co-supervisor) .....

Prof. Dr. Mehmet Yildiz .....

Asst. Prof. Dr. Eralp Demir .....

Asst. Prof. Dr. Bertan Beylergil .....

DATE OF APPROVAL: 05/10/2019

Saher Gul

MFG, MSc Thesis, 2019

Thesis Supervisor: Assoc. Prof. Dr. Burcu Saner Okan

Thesis Co-supervisor: Asst. Prof. Dr. Adnan Kefal

ABSTRACT

EXPERIMENTAL AND NUMERICAL INVESTIGATION OF MECHANICAL EFFECT OF EXTERNALLY WEAK LAYERS IN THICK HYBRID COMPOSITES

SAHER GUL

MFG, MSc Thesis, December 2019

Supervisor: Assoc. Prof. Dr. Burcu Saner Okan
Co-supervisor: Asst. Prof. Dr. Adnan Kefal

Keywords: Thick hybrid laminate composites, Digital Image Correlation, Finite Element Method, Flexural Property

There is a growing interest in the use of thick hybrid composite laminates in the structural elements of aerospace and hydrospace structures. As amount of composite materials used in aircraft structures has now exceeded 50% by weight, it is more crucial than ever to study their mechanical properties and failure behaviors. In the present work, the influence of weak external layers of carbon and glass fibers on the flexural behavior of thick carbon/glass fiber reinforced hybrid composite laminates was examined to monitor their failure mechanisms. In the first part, four types of symmetric laminate structures were designed by tailoring the stacking sequence of glass (G) and carbon (C) fiber reinforced prepregs. Hot Press Curing (HPC) technique was utilized for manufacturing of the laminates. In each composite structure, 48 prepreg plies were used; and their configurations were adjusted to $(C_8/G_8/G_8)_s$, $(G_8/C_8/G_8)_s$, $(G_8/G_8/C_8)_s$, and $(C_8/G_8/C_8)_s$. Flexural tests showed that the highest flexural strength (1260 MPa) was exhibited by the laminate with the configuration of $(G_8/C_8/G_8)_s$, and the highest flexural modulus (79.64 GPa) was shown by the laminate with configuration of $(C_8/G_8/C_8)$. In addition, Digital Image Correlation (DIC) technique was used for the full-field in-plane strain and displacement registration, and for the study of failure mode development during the bending tests. The results indicated that the type of fiber placed along the horizontal midplane of the laminate controlled the failure mode, and the type of fiber available on the faces governed the behavior of stress-

strain curve. The fracture surface characterization performed by optical and scanning electron microscopy techniques indicated that the compressive failures in the form of kink band formation and shear-driven interlaminar delamination were the two most prevalent forms of failure in thick hybrid laminates. In parallel to the experimental study, numerical study was carried out by Finite Element Method (FEM) to investigate the displacement values in the direction parallel and transverse to the loading axis, and for obtaining the longitudinal and shear strain values. Both experimental and numerical studies emphasized the importance of using stacking sequence of a thick hybrid laminate as a practical approach in controlling the flexural properties of the composites. To conclude, this work provides a new insight into the design and fabrication of thick-section hybrid laminates by the adjustment of their stacking sequence.

ÖZET

KALIN HİBRİT KOMPOZİTLERDE DIŞ YÜZEYLERDE ZAYIF KATMANLARIN MEKANİK ETKİSİNİN DENEYSEL VE SAYISAL İNCELENMESİ

SAHER GUL

Yüksek lisans Tezi, Aralık 2019

Danışman: Doç. Dr. Burcu Saner Okan
Eş danışman: Dr. Öğretim Üyesi Adnan Kefal

Anahtar Kelimeler: Kalın hibrit laminant kompozitler, Dijital Görüntü Korelasyonu, Sonlu elemanlar metodu, eğme özelliği

Kalın hibrit laminant kompozitlerin, havacılık ve denizcilik alanlarında yapısal eleman olarak kullanımına yönelik ilgi giderek artmaktadır. Uçak yapılarında kullanılan kompozit malzemelerin miktarı ağırlıkça %50'yi aştığından, bu malzemelerin mekanik özelliklerinin ve hasar davranışlarının incelenmesi önem kazanmıştır. Mevcut çalışmada, cam/karbon takviyeli kalın laminant kompozitlerin dış yüzeylerindeki cam veya karbon fiberli zayıf katmanların eğilme davranışına etkisi hasar mekanizmalarını izlemek için incelenmiştir. İlk bölümde, cam (G) ve karbon (C) elyaf takviyeli prepreglerin istifleme sıralarını değiştirerek dört tip simetrik laminant yapı tasarlanmıştır. Laminant kompozitlerin üretiminde sıcak pres kürleme tekniği kullanılmıştır. Herbir kompozit yapıda 48 tane prepreg katman kullanılmış olup bunların $(C_8/G_8/G_8)_s$, $(G_8/C_8/G_8)_s$, $(G_8/G_8/C_8)_s$, and $(C_8/G_8/C_8)_s$ olarak ayarlanması sağlanmıştır. Eğilme testleri, en yüksek eğilme dayanımının $(G_8/C_8/G_8)_s$ konfigürasyonlu laminant (1260 MPa) ve en yüksek eğilme katsayısının $(C_8/G_8/C_8)_s$ konfigürasyonlu laminantın (79.64 GPa) olduğunu göstermiştir. Ek olarak, tam alanlı düzlem içi şekil değiştirme, yer değiştirme kaydı ve eğme testleri sırasında hasar modu geliştirme çalışması için Dijital Görüntü Korelasyon tekniği kullanılmıştır. Sonuçlar, laminantın yatay orta düzlemi boyunca yerleştirilen elyaf tipinin hasar modunu kontrol ettiğini ve yüzeylerde mevcut olan elyaf tipinin gerilim-gerinim eğrisinin davranışını yönettiğini göstermiştir. Optik ve taramalı elektron mikroskobu teknikleri ile

gerçekleştirilen kırılma yüzey karakterizasyonu, bükülme bandı oluşumu ve kayma tabanlı interlaminar delaminasyon şeklindeki sıkıştırma hasarlarının, kalın hibrit laminantlardaki en yaygın iki hasar şekli olduğunu göstermiştir. Deneysel çalışmaya paralel olarak, sonlu elemanlar yöntemi (FEM) ile yer değiştirme değerlerini yükleme eksenine paralel ve enine doğrultuda incelemek ve boyuna ve kayma gerilimi değerlerini elde etmek için sayısal bir çalışma yapılmıştır. Hem deneysel hem de sayısal çalışmalar, kalın hibrit laminantın istifleme sırasının kompozitlerin eğme özelliklerini kontrol etmede pratik bir yaklaşım olarak kullanılmasının önemini vurgulamıştır. Sonuç olarak, bu çalışma istifleme sırasının ayarlanması ile kalın kesit hibrit laminantların tasarımı ve üretimi hakkında yeni bir yaklaşım sunmaktadır.

To my parents, siblings & friends, who kept me going through the hardest of times.

ACKNOWLEDGEMENTS

I would like to express my gratitude to my thesis supervisor, Assoc. Prof. Dr. Burcu Saner Okan, thesis co-supervisor, Asst. Prof. Dr. Adnan Kefal, and Prof. Dr. Mehmet Yildiz for their guidance in all phases of the thesis, and for their unceasing encouragement and patience.

The financial support provided by the Higher Education Commission of Pakistan for throughout the project is thankfully recognized.

I would like to thank Isa Emami Tabrizi for his support, suggestions and help throughout the project and Leila Haghighi Poudeh for SEM characterization.

Special thanks are due to the very cooperative staff of SU-IMC labs.

I am thankful to my dear friend, Qaisar Khushi Muhammad for his endless help and encouragement.

The moral support and encouragement provided by my family during the course of my master's studies is thankfully recognized.

TABLE OF CONTENTS

LIST OF FIGURES

LIST OF TABLES

LIST OF ABBREVIATIONS

AE	Acoustic emission
BMC	Bulk molded composite
C	Carbon
CCD	Charge-coupled device
CFRP	Carbon fiber reinforced plastic
CTE	Co-efficient of thermal expansion
FRP	Fiber-reinforced polymer matrix composite
G	Glass
GFRP	Glass fiber reinforced plastic
GLARE	Glass laminate aluminum reinforced epoxy
LM	Lunar modules
NDE	Non-destructive evaluation
NDT	Non-destructive testing
PAN	Poly-acrylonitrile
PU	Polyurethane
QFRP	Quartz fiber reinforced plastic
RGB	(Red, Green and Blue)
ROI	Region of Interest

RTM	Resin transfer molding
SMC	Sheet molding compound
SRIM	Structural reaction injection molding
UD	Unidirectional

EXPERIMENTAL AND NUMERICAL INVESTIGATION FOR MECHANICAL EFFECT OF WEAK EXTERNAL LAYERS IN THICK HYBRID COMPOSITES

1. INTRODUCTION

1.1 Composite Materials

Composite materials are multi-phase materials obtained as a result of the artificial combination of two or more constituents, to achieve desirable properties for a specific application. Generally, a composite material is made up of two distinct phases. One is continuous, less stiff and weaker, named as the matrix; whereas the other is discontinuous, more stiff and sturdier, called the reinforcement. The most commonly used modern composite materials are fiber-reinforced composites containing high strength and high modulus fibers in a polymer matrix [1]. In some cases, an additional phase known as the interphase also exists between the reinforcement and matrix due to various chemical interactions or processing effects, as shown in Fig. 1.1.

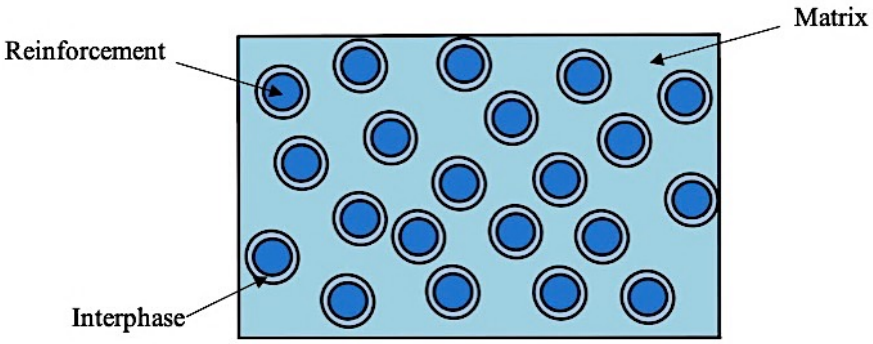

Fig. 1. 1 Phases of a composite material

Numerous factors control the properties of composite materials including the type of reinforcement, matrix properties, geometry, and phase distribution. The homogeneity of the material system depends on the distribution of reinforcement in the matrix. High non-uniformity of reinforcement distribution makes the composite material more heterogeneous, thus increasing the probability of failure in weaker areas. The reinforcement is the main load-bearing component in the composite system [2]. However, the mechanical properties of the composite laminate are mostly controlled by the matrix. The matrix phase protects and supports the sensitive fibers, and also serves the purpose of transferring the load from one fiber to

another. Interphase mainly governs the failure mechanisms, fracture toughness, and stress-strain behavior of composite materials.

1.2 Fiber-reinforced composite materials

Fiber-reinforced composite materials (FRPs) contain high strength and high modulus fibers, either embedded in or bonded to the matrix with a distinct interphase. The presence of a discrete boundary between fibers and matrix allows them to retain their physical and chemical characteristics while delivering a set of properties that are difficult to achieve with the constituents acting alone [3]. The two main types of fibers being used commercially are carbon and glass fibers. These fibers are incorporated in the matrix either in their continuous form (long fibers), or discontinuous form (short/chopped fibers). The matrix material used typically is a polymer and it can have diverse chemical compositions and microstructural arrangements.

Laminate is the most commonly used form of fiber-reinforced composites for structural applications. A number of thin fiber layers and matrix are stacked together and later consolidated into the required thickness to obtain a laminate [4]. The laminated composites' response to the applied loads is direction dependent. In general, the model used for the lamina representation consists of a single fiber per layer. There are three axes, namely, principal fiber direction, in-plane direction perpendicular to fibers, and out-of-plane direction perpendicular to fibers. Fig. 1.2 represents the schematic model of lamina.

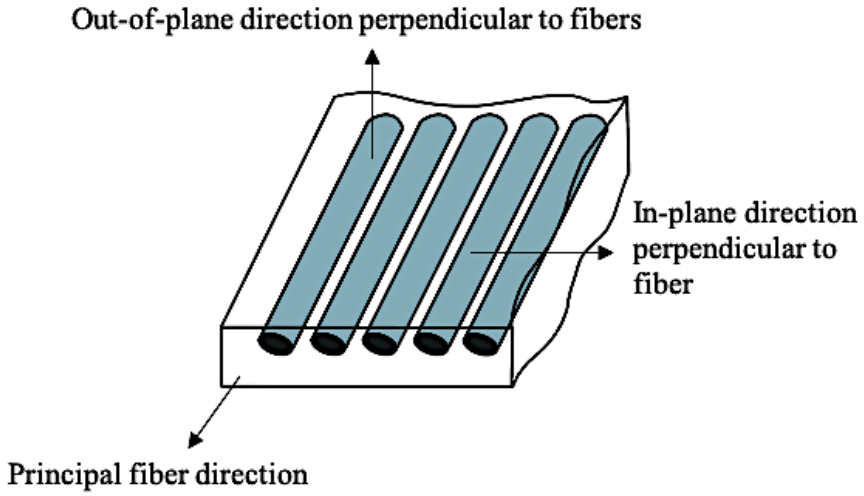

Fig. 1. 2 Schematic model of a lamina

The first high-modulus PAN-based carbon fibers were manufactured in Japan by Shindo [5]. In 1963, carbon fibers with high elastic modulus (600 GPa) were manufactured by British researchers at Rolls Royce [6]. In contrast to the non-conductive nature of the polymer matrix, carbon fibers are electrically and thermally conductive. So, they are used to improve the electrical or thermal conductivity of the matrix. These fibers have almost zero CTE, thus making them a suitable additive to lower the thermal expansion coefficient of the system. Carbon fiber reinforced polymer matrix composites (CFRP) are being used in numerous applications including aerospace, sporting goods, aerospace and even in the field of medicine.

Glass fiber reinforced polymer matrix composites (GFRP) have been in use since the 1940s. They are very strong and lightweight materials, but have a low modulus [7]. They are widely used in the building and construction industry, mostly in the form of cladding for other structural materials, or as a vital part of a structural element. Common examples of GFRP-based products are wall panels, window frames, pipes, ducts, tanks and bathroom units. The industries benefiting the superior properties of GFRPs are the rail transportation, road transportation, aerospace and chemical industry.

1.3 Fiber hybridization in FRPs

A hybrid composite can be defined as a composite material containing two or more different types of reinforcing fibers impregnated in the same matrix to obtain a synergistic effect [8]. Hybrid composites provide the opportunity to tailor the material properties of the laminates according to the application requirements. Fiber hybridization is classified into four different levels, (i) interply hybridization, (ii) intraply hybridization, (iii) interply/intraply hybridization, and (iv) superhybrids. The first type i.e. interply hybrids contain plies from two or more unidirectional composites in a particular stacking sequence. Intraply hybrids include two more different fibers mixed in the same ply. Interply/intraply hybrids have plies of intraply and interply hybrids in a certain stacking sequence, and superhybrids consist of metal foils or metal composite plies within the laminate.

Fiber-hybridization is used to achieve the best cost-to-performance ratio and property optimization of hybrid composites. An improvement of the cost-to-performance effectiveness of the hybrid composites can be realized by sensible selection of different reinforcement types and their optimal placement in critically stressed locations [9]. For instance, in order to reduce

the cost of a hybrid laminate, the amount of carbon fiber content can be reduced whereas, partial replacement of carbon fibers with ductile fibers like glass can be carried out to improve the toughness of the composite [10]. Therefore, for the same volume fraction of fibers, a range of mechanical properties can be achieved using fiber hybridization methods.

1.4 Applications of fiber-reinforced composite materials

The aeronautical, naval and sports industry has leveraged the superior properties of composite materials to its advantage since the 1940s, stimulating a major effort to analyze the structural components made from them. The main drivers behind the use of composites in these industries are; significant weight reduction of the structure, reduced acquisition cost, boosted performance, freedom of design, easy optimization and reduced through-life support. Some common application areas of FRPs are given below.

1.4.1 Aircraft applications

Weight reduction is a critical factor in the aerospace industry, as it helps in gaining higher speeds and increased payloads. FRPs are increasingly being used in the structural components of the aircrafts. CFRP with Kevlar-49 fibers is used in many primary aircraft structures including fuselage, wings and empennage components. These components show high structural integrity and durability. According to one study, the proportion of composite materials in aircraft structures will exceed 50% in the near future [11]. Fig. 1.3 shows some common structural components made up of FRPs in an Airbus® A380 airplane.

1.4.2 Automotive applications

FRPs are used in the automotive industry in three major areas of applications i.e. chassis, engine components and body parts [12]. The parameters of high stiffness, dent resistance and high surface finish are a necessity for the exterior body components of an automobile. Flexible resins (e.g. polyurethane) are used to achieve the acceptable damage tolerance. However, molded composite panels lack in achieving a good surface finish. This issue can be solved by using in-molding coating of the exterior molded surface, like in the case of monocoque of Formula 1 racing car [13]. Impact damage tolerance becomes an area of main concern in the under-body components like the door frames, radiator supports and bumper reinforcement beams, so a careful selection of materials is obligatory. Introduced in 1981, the first major structural application of FRPs was in the chassis component of Corvette rear leaf spring, achieving 80%

weight reduction compared to steel. Another important issue in the automotive manufacturing is affordability, which includes the costs associated with an automobile's complete lifecycle. The high cost of composite materials is currently limiting their adaptation in the automotive industry.

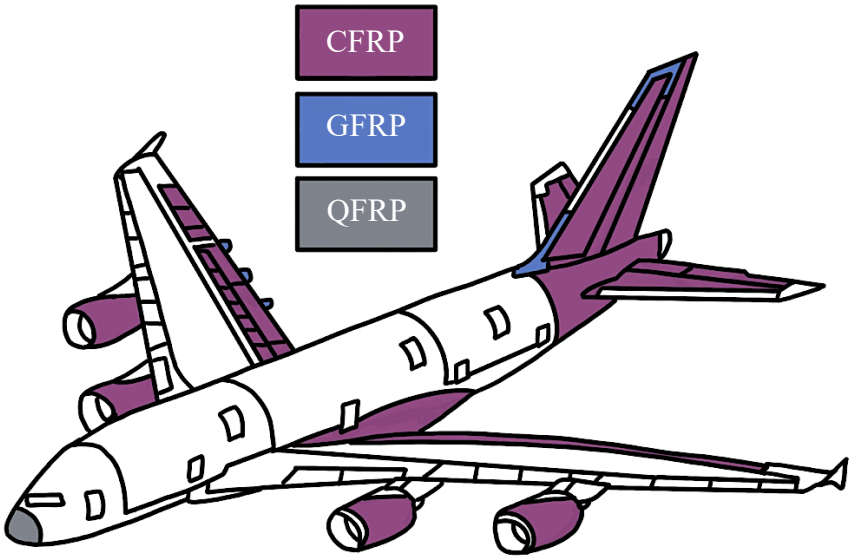

Fig. 1. 3 Use of fiber-reinforced composites in Airbus® A380 [14]

1.4.3 Aerospace industry

The remarkable strength and high strength-to-weight ratio of composite materials makes them very appealing to the aerospace industry. FRPs are preferred in many space vehicles due to the provision of weight reduction of up to 15-25% by selective reinforcement, and 25-50% by using all-composite structures [15]. GFRPs have been used in several manned space vehicles because of their high thermal insulation and endurance against the in-service damage. They were used both internally and externally in the Apollo Command Module. This vehicle transported astronauts to the lunar orbit and back to the earth. FRPs are also being used in lunar modules (LM), transporting astronauts from lunar orbit to the moon surface, and back to the lunar orbit. Various parts like crew compartment ceilings, side panels and electrical covers of LMs are made up of three-ply laminated composites. Other applications of FRPs in the space industry include their use in boosters, satellites and planetary probes.

1.4.4 Sporting industry

Currently, composites are becoming a popular material of choice for improvement of sporting goods. Currently, approximately 10% of the total advanced fiber consumption goes into sports and recreational applications. Pole vault jump bars, boat hulls and finish poles were among the earliest sports goods constructed using composites materials [16]. However, currently the range of applications is much diverse. Tennis rackets, golf clubs, boat oars, board rackets, surfboards, skis, ski poles, archery instruments and bicycles are some examples where the structural element is made up of a composite material.

1.4.5 Marine industry

The use of FRPs in maritime structures is widespread. These structures are designed for service in an adverse environment, and two conditions are to be met for an acceptable performance: (i) knowledge of the composite material's behavior in water, and (ii) validation of the structural components by laboratory testing to ensure their safety. Polymeric composites are used for the construction of modern ships with more efficient fuel consumption and maneuverability. Maritime industries prefer these materials because they are corrosion-free and water-resistant. For example, in speedboat Revolve-42, the main hull and deck are made up of composite laminates, helping the boat to reach speeds up to 125 km/h [17]. Similarly, sandwich composite structures with a honeycomb core are being used in the manufacturing of the wing of Vestas Sail-rocket 2 sailboat. Thermoplastic-matrix composites are widely used in the manufacturing of large elements of submarines, as they offer better performance compared to their conventional counterparts. Yachts, boats, small ships, passenger boats, and structural elements like the cabin, bulwark and roof are constructed using polymer matrix laminates.

1.5 Manufacturing techniques for fiber-reinforced composite materials

The manufacturing techniques for fiber-reinforced polymer matrix composites are categorized into seven major processes:

i. Molding
ii. Casting
iii. Thermoforming
iv. Expansion
v. Coating
vi. Fabrication

vii. Radiation

Different sub-techniques can be used within each of these processes (Fig. 1.5). Within the scope of current project, the polymer matrix used is a thermoset resin; therefore, only methods specific to thermoset polymers have been discussed in detail in this section. Even though manual production processes are time-consuming, but they are also among the simplest methods. Following are the most commonly used methods of composite manufacturing [18]:

1.5.1 Hot pressing

The easiest method of fabricating a high-performance composite flat plate is to use a process called hot pressing. This method involves simultaneous application of heat and uniaxial pressure and is mostly used for the manufacturing of simple shapes, like plates and pellets. The main parameters of a hot-pressing process include: (i) pressing temperature, (ii) pressing pressure and, (iii) matrix curing time. Usually a mold is used for the compensation of thermal expansion of the matrix, and to maintain the shape of the part during application of pressure. A schematic representation of a simple hot press machine has been shown in the following figure.

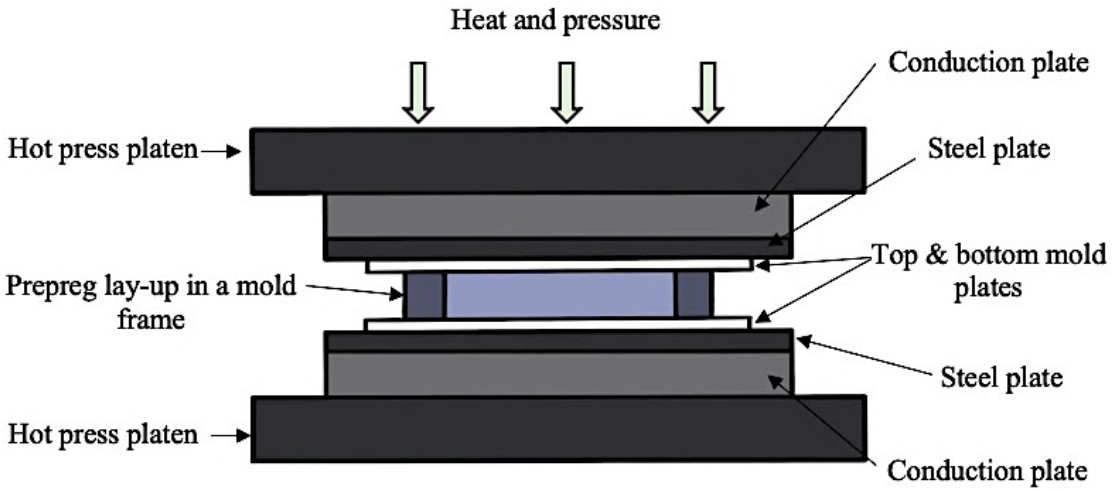

Fig. 1. 4 Schematic of a hot press machine

As evident from Fig. 1.4, a hot press machine contains numerous parts like the conduction plates, steel plates, mold plates and platens. The prepreg lay-up is placed inside the mold and a uniaxial pressure is applied uniformly by the top platen. The amount of pressure and curing time depends upon the properties of the polymer matrix.

1.5.2 Autoclave-based methods

Autoclave molding is used where high surface quality is required. This process enables the manufacturing of compact and void-free parts, as the method uses an autoclave to provide high pressure and heat to the composite laminate during the resin cure cycle. Mostly, a composite prepreg is used for autoclave molding. The components of an autoclave machine include a mold, releaser, peel ply, bleeder, breather and a vacuum bag. Layers of prepreg are laid up in the required fiber orientations on the molding plate until the requisite thickness is achieved. Pressure is applied to press the prepregs against the molding plate, subsequent heating hardens the matrix and the part gets the required shape.

Better surface finish is achieved by using peel plies at the top and bottom prepreg layers. Excess resin during curing is absorbed by the layers of bleeder and breather cloth. The whole assembly is vacuum bagged for the removal of any entrapped air between the layers. Finally, the mold and the composite laminate part with vacuum bag is transferred into an autoclave for curing. The process is mainly used for making aircraft parts, spacecraft and components for military applications.

1.5.3 Resin Transfer Molding (RTM)

High-performance thermosetting composites are manufactured using resin transfer molding. In this method, a pre-shaped reinforcement material in the shape of the final product is kept in the lower half of the mold. The upper mold is then closed onto the lower mold. High pressure and temperature are applied while the resin is injected into the mold. Due to the high pressure used, resin easily impregnates the reinforcement, and the volatile gases escape out of the mold through the vents as shown in Fig. 1.6.

The curing cycle is controlled by the thickness of the laminate and the matrix type. Rapid manufacturing of large and complex shaped parts is possible through this technique. Fiber geometry, fiber content, applied pressure, mold temperature and resin viscosity are the factors affecting the quality of the final product.

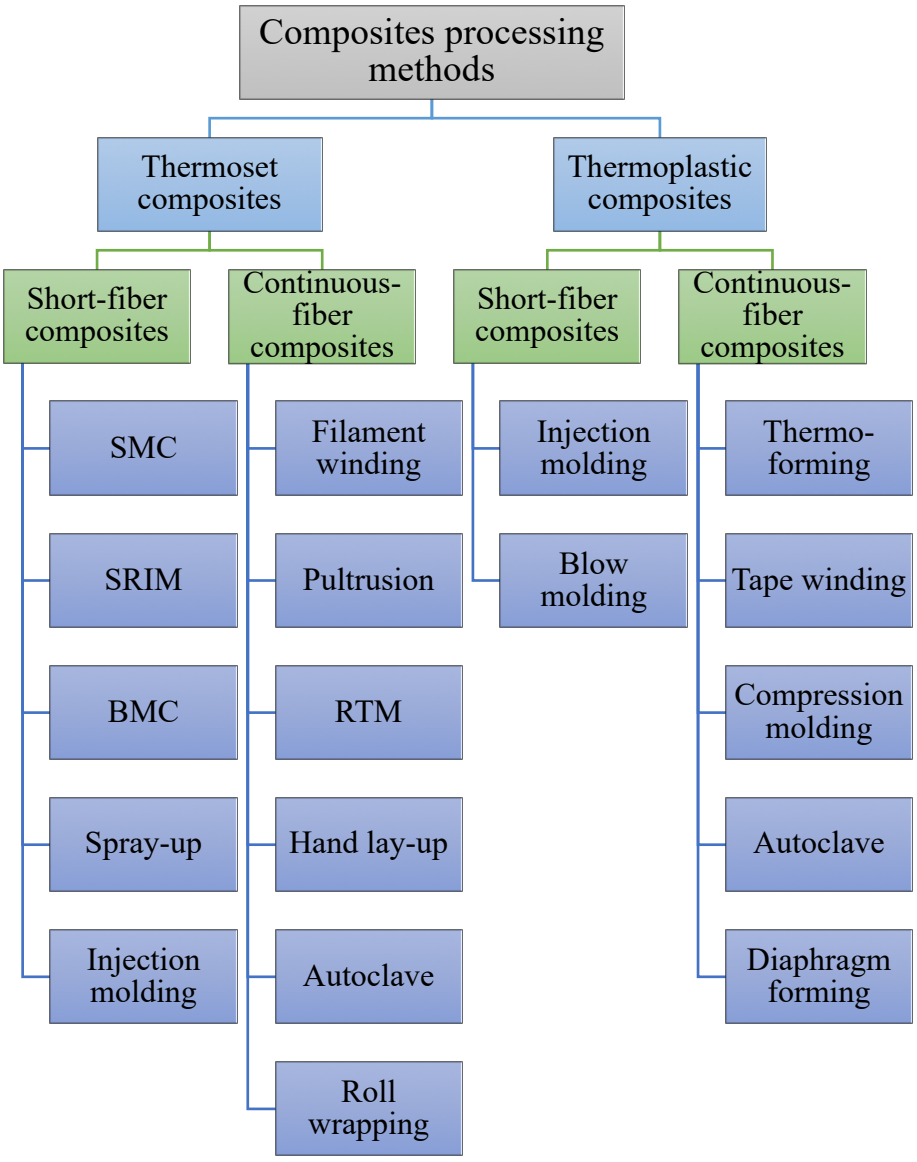

Fig. 1. 5 Manufacturing processes for polymer matrix composites [8]

The main advantage of this method is the achievement of good surface finish on both sides, improved control over the part thickness, shorter cure cycles, less volatile emissions, and efficient consumption of fiber and resin. However, a few drawbacks include the high cost of tooling, complex shapes of the mold cavity, and unsuitability for high viscosity resins. Common areas of application for RTM include automotive, aerospace and sports industries.

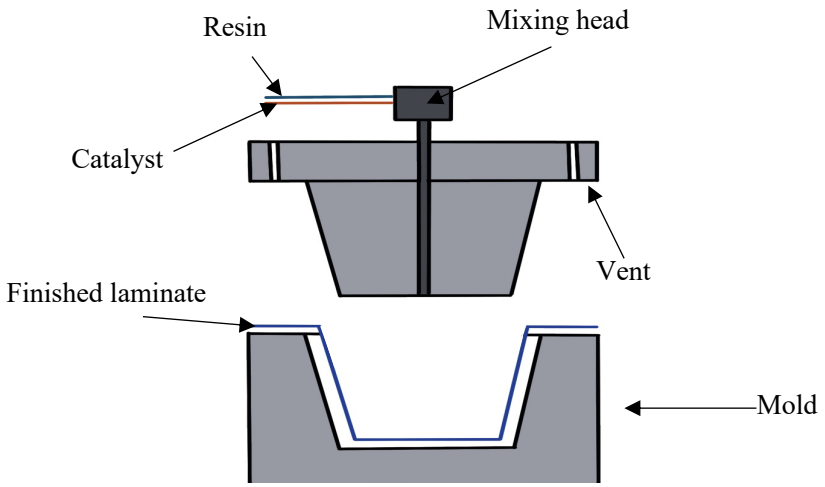

Fig. 1. 6 Resin transfer molding process

1.1.1 Vacuum bagging process

The vacuum bagging process utilizes a vacuum pressure during the resin cure cycle. Resin and the fibers are held in the desired location by using atmospheric pressure. An airtight bag is used to seal the laminate, and all the air is evacuated out of the bag using a vacuum pump. The process contains different components, like the mold, releasing agent, prepreg lay-up, peel ply, bleeder, releasing film, breather and a vacuum bag. A clean surface for bonding purposes is achieved using a peel ply.

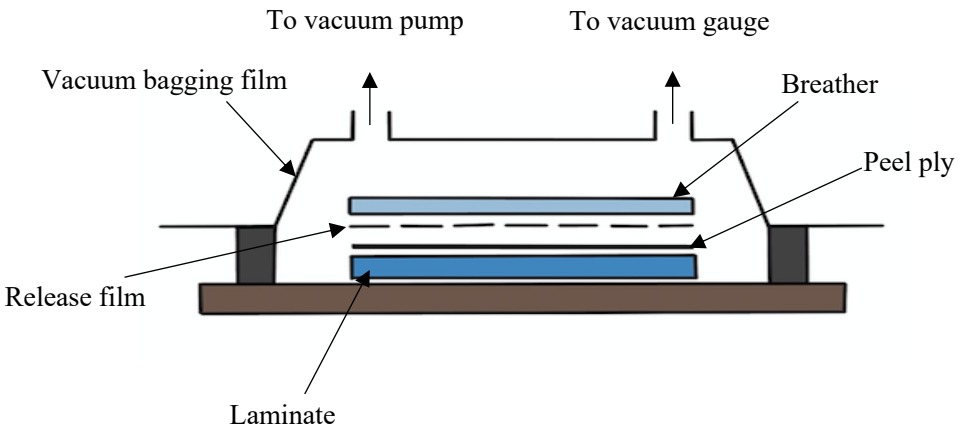

Fig. 1. 7 Vacuum bagging process

Resin is prevented from sticking to the mold surface by using an appropriate releasing agent. Sealant tapes are present on both sides of the bag to provide a vacuum-tight seal between the bag and the mold surface. Excess resin is usually absorbed by using a bleeder layer. The perforated releasing film allows passage to entrapped air and volatile materials. Uniform pressure around the part is ensured by the use of a breather. Heat and pressure are applied for a specific time depending upon the cure cycle of the matrix. This process has various advantages including achievement of higher fiber volume fraction, good adhesion, low volatile emissions and reduced mold costs. Fig. 1.7 shows a schematic representation of vacuum bagging process.

1.1.2 Hand lay-up

The most commonly used method for the fabrication of composite laminates is the hand lay-up method. Usually continuous fibers in the form of knitted, woven, stitched or unidirectional fabrics are used. In this method, placement of alternate layers of matrix and reinforcement material is done by hand. A releaser is usually applied on the mold surface for an easy removal of the manufactured part.

Matrix is pressed on the reinforcements using a roller which simultaneously removes the extra resin from each layer, ensuring the uniform distribution of resin over the surface. The process is repeated for all layers of reinforcement material until the required thickness is achieved. The matrix is then left to cure (usually for 24 h) and subsequent removal of the part from the mold is performed.

1.2 Tests for measuring interfacial strength in composite materials

Characterization of the interfacial strength of the fiber/matrix interface is conducted by numerous methods including, flexural tests, single fiber pull-out tests, curved-neck specimen test, instrumented indentation tests, fragmentation test and laser spallation technique [19]. Within the scope of the current project, bending properties of hybrid composites were studied, so only the three-point bending test is explained in detail in this section.

1.2.1 Flexural tests

Flexural or bending tests are easy to perform and provide a semi-qualitative idea of the interfacial strength of fiber/matrix interface of a composite material. For an elastically stressed simple beam in bending, there are two basic governing equations:

$$\frac{M}{I} = \frac{E}{R} \tag{1.1}$$

and

$$\frac{M}{I} = \frac{\sigma}{y} \tag{1.2}$$

Where M is the applied bending moment, I is the 2nd moment of area of the beam section about the neutral axis, E is the Young's modulus of elasticity of the material, R is the radius of curvature of the beam in bending, and σ is the tensile or compressive stress on a plane distance y from the neutral plane. For a circular beam,

$$I = \frac{\pi d^4}{64} \tag{1.3}$$

where d is the diameter of the circular section beam. For a beam of a uniform, rectangular section, the value of I changes to,

$$I = \frac{bh^3}{12} \tag{1.4}$$

where b is the width of the beam and h is the beam height. h and y are measured in the same direction as the bending takes place in the direction of the depth. If a beam has a symmetrical section with respect to the neutral plane, using $h/2$ instead of y in Eq. (1.2) provides the stress at the beam surface. The stress and strain vary linearly with the thickness y when an elastic beam is bent. In an elastic regime, stress and strain are related by

$$\sigma = \mathrm{E}\varepsilon \tag{1.5}$$

The following simple relation can be obtained from Eq. (1.1), (1.2), and (1.5),

$$\varepsilon = \frac{y}{R} \tag{1.6}$$

where ε is the strain in the bent beam.

1.2.1.1 Three-point bending test

A schematic representation of a three-point bending test has been given in Fig. 1.8. This test is the simplest and most widely used type of flexural tests. The bending moment M in a three-point bending test is given by,

$$M = \frac{SP}{4} \tag{1.7}$$

where, P is the applied load, and S is the span length of the specimen. In this test, the bending moment is maximum at the mid-point of the specimen. Maximum stress for a rectangular beam is given by,

$$\sigma = \frac{3SP}{2bh^2} \tag{1.8}$$

The direction of fibers can be parallel or transverse to the specimen length. In a three-point bending test, the shear stress is constant. The maximum load (P_{max}) relates to the maximum shear stress ($\tau_{\max}$) by,

$$\tau_{\max} = \frac{3P_{max}}{4bh} \tag{1.9}$$

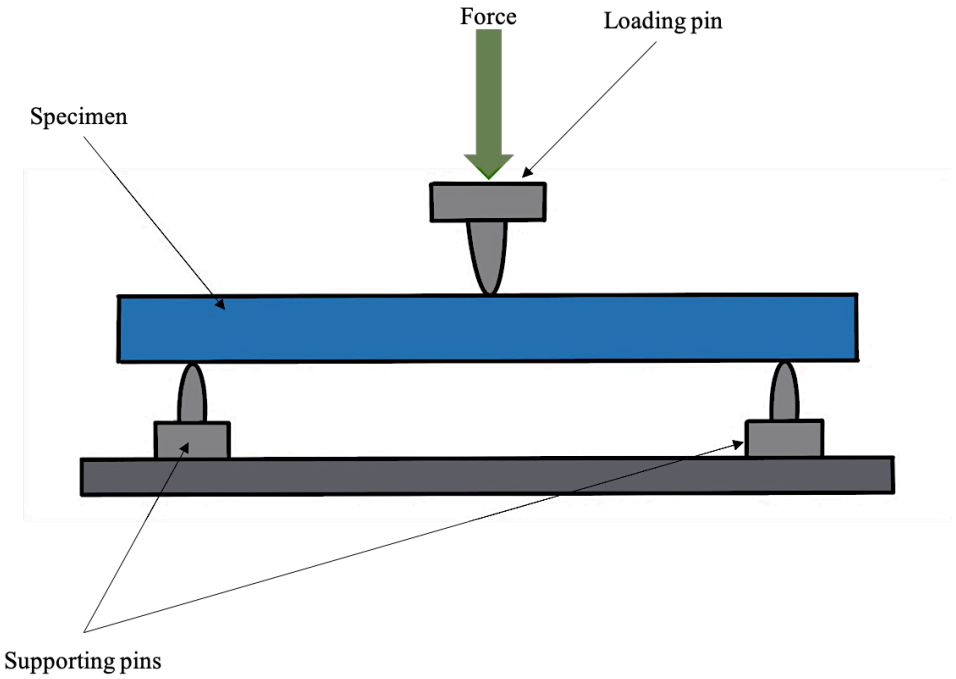

Fig. 1. 8 Schematic representation of a three-point bending test

1.3 Non-destructive characterization of composite materials

Often composite materials are structurally complex and formed by a number of layers. Delamination or disbands (laminate-to-laminate or laminate-to-core), broken fibers due to impact, missing adhesives, inadequate curing, voids, porosity and microcracking instigates a loss of mechanical properties of composite materials. The evaluation and detection of these damages in composites is restricted by the fact that the damage is often not visible to the naked eye, thus making its analysis rather challenging. The field of Non-Destructive Evaluation (NDE) or Non-Destructive Testing (NDT) entails the identification and characterization of damages present on the surface and interior of the material, without altering the component or cutting the part [20]. Numerous techniques available for the NDT include infrared

thermography testing, ultrasonic testing, radiographic testing, acoustic emission testing, optical testing, digital image correlation, electromagnetic testing, magnetic particle testing, and liquid penetrant testing. These methods are categized into contact and non-contact methods. For the current project, digital image correlation was used for obtaining the full-field displacement and shear strain maps.

1.3.1 Digital Image Correlation

Digital Image Correlation (DIC) is a full-field contact-less optical method for the measurement of displacements in the experimental testing. It was originally developed in the early 1980s [21]. DIC is based on the correlation of the digital images taken during the execution of a mechanical test. The pictures taken during the test are converted from RGB color space to greyscale and treated as a matrix. Each element of this matrix corresponds to a pixel, which represents one specific point of the specimen surface. The intensity of color (from black to white) determines the value of each pixel. Fig. 1.9 provides a schematic of DIC.

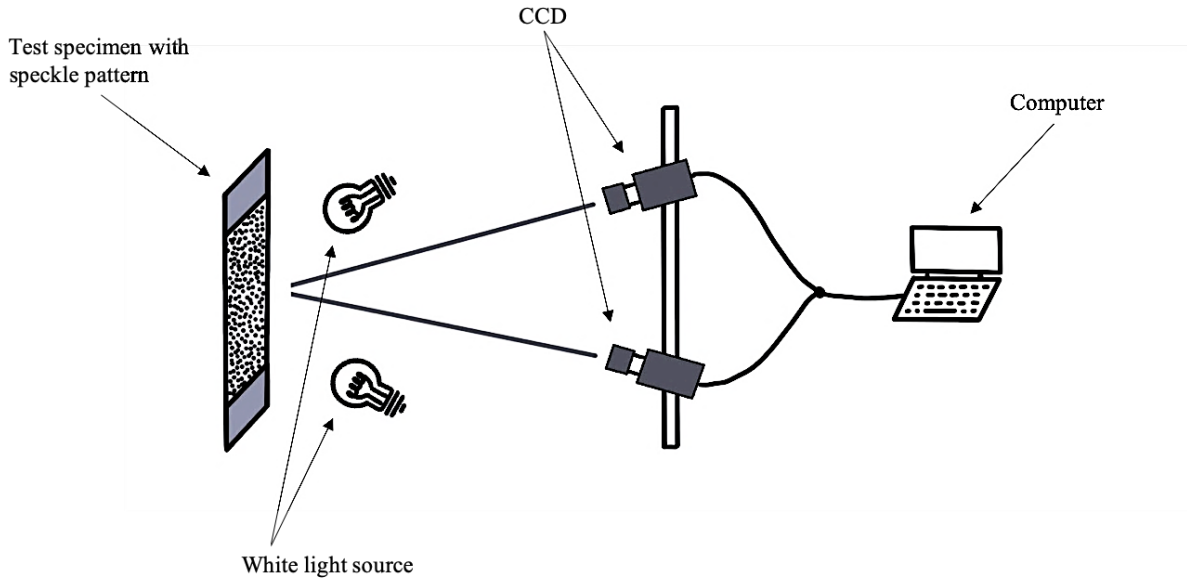

Fig. 1. 9 Schematic of a DIC technique

A computational grid is defined on part of a picture or the whole picture, named as the Region of Interest (ROI), for the calculation of in-plane displacement of the specimen surface. The pictures taken before and after the deformation are correlated. Matching of the points in

the grid in ROI is done by associating the position of points to the peak of the correlation coefficient after the deformation of the sample. Depending on the computational effort required in the calculations, different correlation criteria can be used. The reliability of correlation can be improved by a correlation of two subsets of pixels. Subsets are either square or circular with their size ranging from 5 pixels to 50 pixels. The properties of the speckle pattern determine the subset size to be used.

The displacement of each point of the grid corresponds to the relative distance between its position in the deformed and the undeformed image. DIC results are initially computed in pixels and later converted into millimeters. The conversion factor (pixel to millimeter) can be determined from the focal length and the distance of area of interest on the specimen surface to the optical sensor. Firstly, the method gives measurements with resolution of 1-pixel size, but sub-pixel interpolation algorithms can provide a resolution up to $1/100^{th}$ of the pixel. Finally, the discrete displacement field obtained directly by this procedure is interpolated with pre-defined shape functions.

Preparation of the experimental setup for DIC application needs special attention. A speckle pattern, consisting of white and black dots randomly distributed over a white background is produced on the specimen surface using an airbrush or spray painting. The accuracy of the results is related to the size of the spots. In the case of a rough specimen surface, the natural surface texture is sufficient for providing ample contrast, so no additional preparation is required. To minimize the measurement error, the high-resolution camera is to be used and placed on a rigid frame. Parallelism is ensured between the specimen surface and the sensor. Finally, the lighting conditions are to be kept even and stable during the execution of the test.

1.3.2 Acoustic Emission testing (AE)

Acoustic emission is an efficient method for the analysis of faults in a composite material. When materials are thermally or mechanically stimulated, they release stress-waves. For the detection and localization of activity areas, AE testing uses stationary piezoelectric sensors on the specimen surface [22]. On stimulation, these activities indicate discontinuities, which are represented and analyzed according to AE parameters. The existence of discontinuities in the initial stages is detected by the method, which allows an analysis of the whole surface of the specimen in one test. AE method allows the testing to be performed during operation. Every

acoustic emission consists of elastic waves, which can be recorded as wave forms. The mechanical vibrations of elastic waves are converted into electrical signals, which can later be characterized by various signal processing tools. These tools are categorized into waveform-based features and wave energy-based features. Fig. 1.10 depicts a schematic of AE testing.

The emitted acoustic signal depends on the characteristics of the source located inside the material. Different AE waveforms are produced by different AE sources. Even the same AE source mechanism can produce different signals if the source is oriented differently with respect to the medium geometry or the path of propagation to the detector. However, in spite of these limitations, AE monitoring has benefits in comparison to other NDE methods. For example, the use of an array of AE sensors can enable the monitoring of a global region or volume of the material, eliminating the need of expensive point-to-point scanning. AE can also be used in-*situ* for monitoring a structure in service, thus providing huge economic advantage and improved safety of the parts.

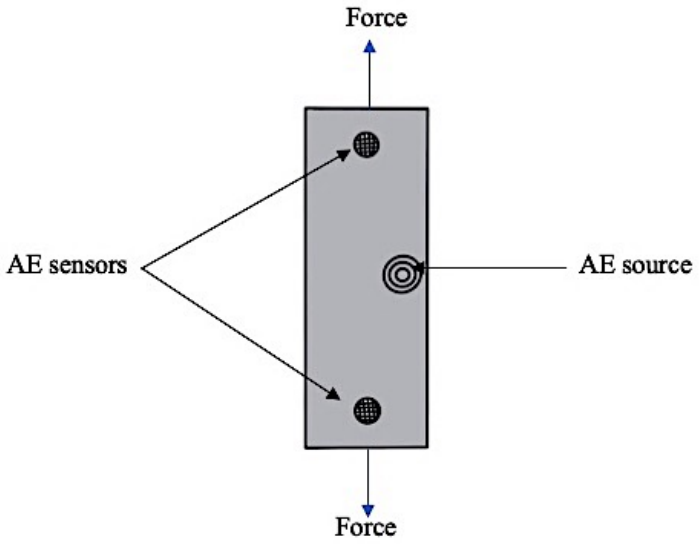

Fig. 1. 10 Schematic representation of Acoustic Emission (AE) method

1.4 Motivation

Structural composites offer a great advantage of design flexibility, i.e. the opportunity to tailor the material as per optimal requirements of the structure. The mechanical behavior of the composite is governed by the matrix properties and the type of reinforcement [1]. Fiber-reinforced polymer matrix (FRP) composites are an emerging class of composite materials, containing high strength and high modulus fibers as reinforcing agents [23]. There is a growing

interest in the fabrication of FRP composites and their optimization by applying various manufacturing processes including; resin transfer molding, compression molding, hand lay-up and autoclave-based methods [24], [25]. FRP composites are primarily used to improve the mechanical and tribological properties of structures used in numerous industries like the aerospace, transportation and defense industry; with aerospace being the primary consumer.

In FRP composites, carbon and glass fibers are the most commonly used reinforcing agents. Carbon fiber reinforced polymer matrix composites (CFRP) are extremely lightweight and high-performance materials offer weight reductions up to 60% compared to their conventional counterparts, like metals and ceramics. CFRPs also have excellent corrosion and bursting resistance, making them suitable for a myriad of applications; including construction materials, wind power generation and energy applications. However, the high cost involved in the manufacturing of CFRPs and low fracture toughness is constraining their implementation in traditional engineering fields [26]. Due to the inherent brittleness of carbon fibers, CFRP-based structures are vulnerable to stress concentrations [27]. The gradual accumulation of minor cracks in carbon fibers can severely damage the structure in the form of delamination or matrix cracking. The poor residual strength of the structure and lack of ductility in carbon fibers can eventually result in a catastrophic failure without any prior warning [28]. To overcome these issues in CFRPs, an ingenious method is to manufacture a 'hybrid' composite, wherein, one or more types of fibers are used in a common matrix to obtain a synergistic effect through design and structural optimization [10], [29]. An appropriate hybrid material candidate for CFRPs in this case is the glass fiber because of its higher strain-to-failure ratio compared to the carbon fibers, especially in unidirectional composites. So, the carbon/glass fiber reinforced hybrid composites produced as a result of 'fiber hybridization' have improved strength and high fracture toughness compared to CFRPs.

Improvement of the cost-performance effectiveness of the hybrid composites can be realized by sensible selection of different reinforcement types and their optimal placement in critically stressed locations [9]. For instance, the cost reduction in a hybrid composite is achieved by decreasing the amount of carbon fibers in the structure [10]. In one of the recent work, Chen *et al.* [30] found that the placement of carbon layers on both the tensile and compressive sides of the specimen can cause an increase of 2.5 times in the flexural modulus compared to an all-glass composite. In addition, Zhang *et al.* [31] reported that the flexural

strength increases from 218 MPa to 339 MPa by the placement of carbon fibers on top and bottom surfaces of a hybrid composite. Song *et al.* [32] and Jesthi *et al.* [33] reported an improvement in tensile strength by using carbon fibers near the mid-plane of the carbon/glass hybrid structure. Moreover, Prusty *et al.* [28] noted that with 51% carbon fiber content, the strength of a hybrid composite can reach 96% of an all-carbon composite; thus considerably reducing the cost without a significant loss of mechanical properties. In the light of aforementioned studies, it can be concluded that the same volume fraction of fibers can provide a range of mechanical properties through the use of inter-ply hybridization in composites.

Among the mechanical properties, the flexural property remains a vital factor in composite design. Flexural response of hybrid laminates depends on the type of hybridization and fiber orientation. Recently, Tabrizi *et al*. [34] demonstrated that the use of carbon fibers on the external layers in a thin carbon/glass fiber hybrid composite can increase the flexural modulus of the laminate up to 3 times compared to an all-glass composite. Wei *et al.* [35] observed an increase of 300% in the flexural strength of the specimen, when the principal fiber direction was changed from 90° to 0° in a hybrid composite. Sudarisman *et al.* [36] found that with the change of span-to-length ratio from 16:1 to 32:1, flexural strength of the carbon/glass hybrid is increased. Based on several other studies [37]–[42], it can be established that the flexural behavior of a hybrid composite is controlled by: (i) compression properties of the upper layers, (ii) tensile properties of the lower layers, (iii) span-to-depth ratio, (iv) stacking sequence, (v) laminate thickness and, (vi) fiber orientation.

While the flexural response of thin laminates; and fatigue, compression and impact response of the thick hybrid composite laminates has been extensively studied [43], [44], [53]–[55], [45]–[52], yet the study of flexural behavior of thick laminates (with thickness > 6mm) is still challenging. The increased use of the thick composites in vital engineering structures demands a comprehensive characterization of their static and, especially dynamic mechanical and failure behavior. At the design stage of composite structures, it is very crucial to formulate theories for the prediction of transverse shear deformations and through-the-thickness strain and stress fields. 3 distinct types of plate theories have been formulated over the course of last few decades, namely Equivalent Single Layer (ESL) theory, Layer-Wise (LW) theory and the Zigzag (ZZ) theory [56]. In the Zigzag models, the axial displacement pattern provided by elasticity solution is employed to define a zigzag displacement function of each layer [57].

Refined Zigzag Theory (RZT) is an improved version of ZZ theory and is based on the kinematics of first-order shear deformation theory. Being a displacement-based theory, RZT efficiently predicts the true stress and strain results of laminated structures with highly heterogenous behavior and has an effective finite element implementation [58]. Although the research of RZT theory application has risen over the recent years, however its application in the fiber-reinforced hybrid laminates is still understudied.

Albeit all the studies delineated above, to date, there is no study to investigate the role of external layers in controlling the flexural behavior of carbon/glass fiber reinforced thick-section laminates using DIC and FEA as complementary techniques. To address this issue, the current study aims to analyze the effect of interlayer hybridization on the flexural behavior of carbon/glass fiber reinforced hybrid laminates with a nominal thickness of 10.92 mm. Four hybrid carbon/glass composites are manufactured using hot press technique. The flexural properties and failure sites of the composite specimens are investigated in detail by optical microscopy and scanning electron microscopy. Additionally, FEM is utilized to validate the the experimental study of flexural behavior of thick-section hybrid laminates.

2. MATERIALS AND METHODS

2.1 Materials

Unidirectional (UD) carbon fiber reinforced epoxy resin prepreg (KOM10 34700 HTCF UD300 37% 600KOMP) and UD glass fiber reinforced epoxy resin prepreg (KOM10 WR6 2400TEX EGF UD300 35% 600KOMP) were purchased from Kordsa Teknik Tekstil A.S. (Turkey). The resin system for both types of prepreg was OM10. Carbon fiber and glass fiber prepregs had resin content of 37% and 40% respectively.

2.2 Composite manufacturing by hot press technique

2.2.1 Design and configuration

The carbon fiber and glass fiber prepregs were cut into dimensions of 300 × 300 mm using ply cutter (ZUND G3-L3200). After cutting, manual stack-up of uncured prepregs was done in 0° orientation with configuration of $(C_8/G_8/G_8)_s$, $(G_8/C_8/G_8)_s$, $(G_8/G_8/C_8)_s$, $(C_8/G_8/C_8)_s$, G_8 and C_8 designated as 1C-UD, 2C-UD, 3C-UD, 13C-UD, AG-UD and AC-UD respectively (Fig. 2.1).

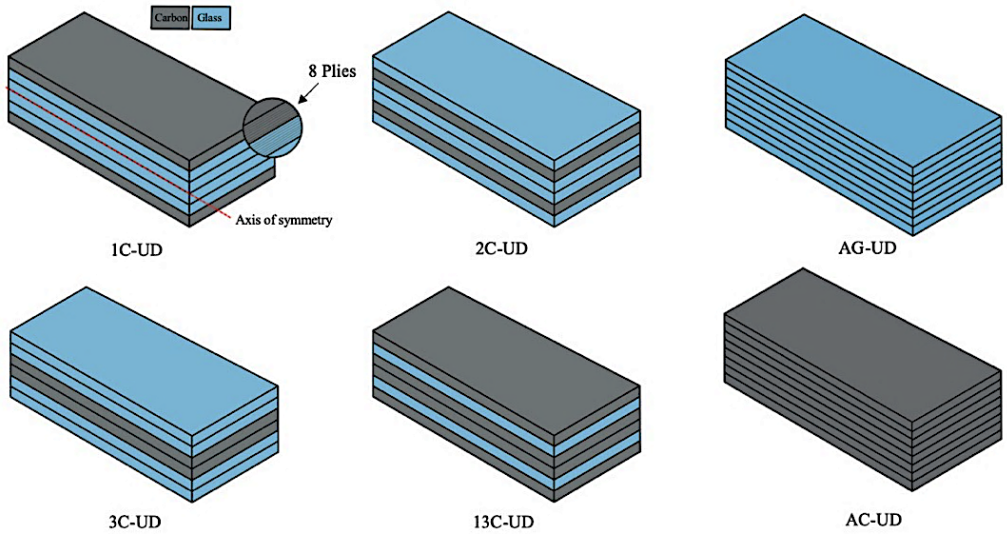

Fig. 2. 1 Stacking sequences used for carbon/glass fiber reinforced hybrid composite manufacturing

2.2.2 Manufacturing of composites

After stacking of uncured prepregs, a steel mold (300 × 300 mm) was prepared. The mold was first cleaned with ethanol, and then 3 layers of sealing agent (XTEND 838) and 1 layer of releasing agent (XTEND CX-500) were applied to the mold surface. There was a time interval of 15 minutes between the application of each new layer to ensure proper drying of previous layers. Steel mold was used for optimal compensation of material compaction and thermal expansion during cure cycle. A manual hot press (MSE Teknoloji Ltd. Turkey) was used for curing of the stacked prepregs. According to the technical data sheet provided by the prepreg manufacturer, following steps for the curing were followed as: (i) hot press was heated to 20 ℃ before putting the steel mold inside, and pressure was kept at 0 bar. (ii) temperature was gradually increased to 120 ℃ with 2-3 ℃ increase per min, while the pressure was gradually increased to 6.4 bars (iii) temperature and pressure were maintained at 120 ℃ and 6.4 bars respectively for 1 h (iv) for the cooling cycle, temperature was gradually lowered down to 80 ℃ at the rate of 2-3 ℃ per min before releasing the pressure. The manufactured hybrid laminates had a thickness in the range of 10.92 mm-11.88 mm. AG-UD and AG-UD (specimens with 8 plies) had a thickness of 2.28 mm and 1.65 mm respectively. All of the hybrid composites were symmetric about the mid-plane, containing a total of 6 layers with each layer comprising of 8 plies of the respective material (Fig. 2.1).

2.3 Mechanical testing

2.3.1 Tensile tests

According to ASTM D3039 standard [59], five tensile test specimens (250 × 15 mm) in the fiber direction i.e. 0 ° direction, and five tensile test specimens (175 × 25 mm) transverse to the fiber direction i.e. 90 ° direction were cut from the AC-UD and AG-UD laminates using 3-axis milling machine (Poysan 354-90). Using an 800-grit sandpaper, the edges of test specimens were polished in order to eliminate any extrusions on the peripheral of bars. In accordance with ASTM D3039 standard, carbon tabs with a size of 56 × 15 mm (for a specimen with 0 ° fiber direction), and 25 × 25 mm (for a specimen with 90 ° fiber direction) were adhered to the grip locations of respective AC-UD & AG-UD test specimens with Araldite® glue. Strain gages (Vishay PG) with gage factor of 2.16 ± 1% were attached to the middle of the test specimens to obtain Poisson's ratio and strain value. Tensile testing was conducted on Instron® 5982 Universal Testing Machine with a load cell of 100kN. The test speed was set to 2 mm/min.

Tensile tests were performed until the global failure of specimens occurred. The tests were conducted at the standard testing conditions (temperature, 23± 2 ℃; relative humidity, 50% ± 10%).

2.3.2 V-Notch Shear tests

According to ASTM D5379 standard [60], five shear test specimens (76 × 20 mm) in the fiber direction and five shear test specimens (76 × 20 mm) transverse to the fiber direction were cut from the AC-UD & AG-UD laminates using 3-axis milling machine (Poysan 354-90). Strain gages (Vishay PG) with a gage factor of 2.16 ± 1 % were attached to the middle of the test specimen to obtain strain value. V-Notch shear tests were performed on Instron® 5982 Universal Testing Machine with a load cell of 100kN. The test speed was set to 2 mm/min. Shear tests were performed until the strain value of 5% or global failure was achieved by the specimens. The tests were conducted at the standard testing conditions (temperature, 23± 2 ℃; relative humidity, 50% ± 10%).

2.3. 2 Flexural tests

For the flexural test, test samples in the fiber direction (0 °) from 1C-UD, 2C-UD, 3C-UD and 13C-UD laminates were cut according to dimensions mentioned in ASTM D790-A standard [61] using the water-jet machine (KUKA KR16 F). The specimen dimensions are given in Table 2.1. The flexural tests of the samples were conducted on Instron® 5982 Universal Testing Machine with a 10 kN load cell. The crosshead speed was set to 2 mm/min.

Table 2. 1 Specimen dimensions for ASTM D790-A 3-Point Bending Test

Sr. No.	Sample	Width	Span length	Total specimen length (including overhanging on both sides)
		mm	mm	mm
1	1C-UD	41.94	167.77	201.33
2	2C-UD	45.96	183.85	220.62
3	3C-UD	46.96	187.84	225.40
4	13C-UD	47.56	191.84	230.20

The L/d (support span length to thickness) ratio was kept 16/1 for all samples. The tests were conducted at the standard testing conditions (temperature, 23± 2 ℃; relative humidity, 50% ± 10%).

2.4 Fracture Surface Characterization

The fracture surfaces of the laminates were studied using a NIKON® SMZ 800N stereo optical microscope and Leo Supra 35VP Field Emission Scanning Electron Microscope (SEM). Samples for SEM characterization were prepared using a precise cut-off machine (Struers Discotom-10) with dimensions of 2 × 2 cm. The disintegration of the fractured specimens was prevented during specimen preparation.

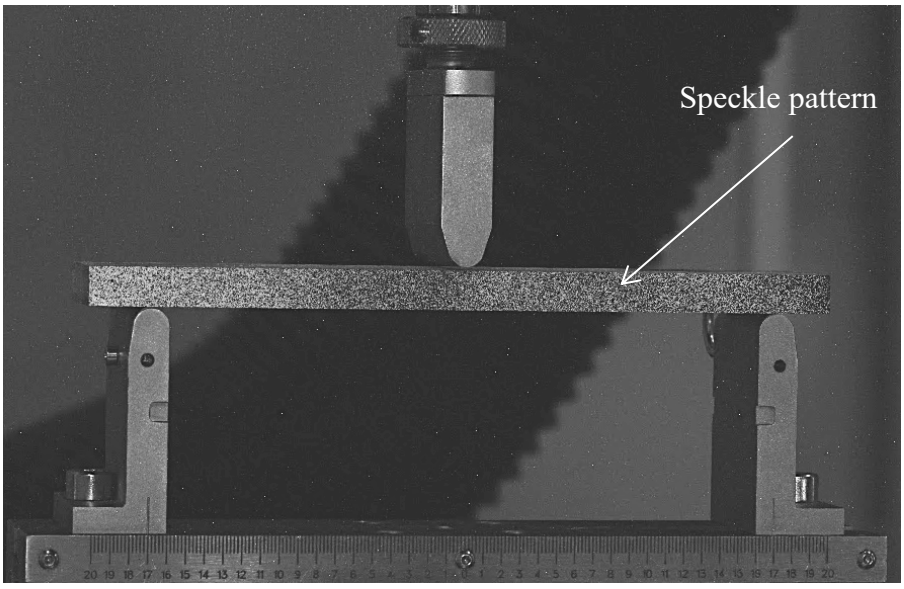

Fig. 2. 2 Flexural test specimen with speckle pattern

2.5 Digital Image Correlation

The local strains on the surface of flexural test specimen were monitored and measured by using Digital Image Correlation (DIC) with GOM (Braunschweig Germany) 12M sensor system. Using black (RAL-9005) and white (RAL-9010) spray paints, the specimen surface was speckle patterned throughout the gage length (Fig. 2). Calibration was done according to a 250 × 200 mm calibration object, as per the manufacturer's directions. Using the ARAMIS software, the surface pattern quality was inspected before the start of the flexural test. For tracking the speckle pattern during the flexural test, a facet size of 25 pixels and a step size of 19 pixels was used.

Displacement of the speckles during flexural test was used to obtain the Lagrangian strains, deformation maps and strain maps of the specimens by using ARAMIS software.

2.6 Finite element models of the bending experiments

The 3-point bending test was simulated using a commercial Finite Element Analysis (FEA) tool of ANSYS®. The area between the supports (span length × width) of the specimen was discretized using 43470 solid elements with 156492 Degree of Freedom (DOF). The mesh pattern for the bending specimen is shown in Fig. 2.3. The orthotropic material properties for AC-UD & AG-UD samples are given in Table 2.2. Using ASTM D3039 and ASTM D5379 standards, the Young's moduli E_{11}, E_{22} and E_{33}, in-plane shear modulus G_{12} and Poisson's ratio v_{12} of both all-carbon and all-glass fiber reinforced laminates were obtained. For both types of specimen (AC-UD & AG-UD), it was assumed that $G_{13} = G_{12}$ and, $v_{13} = v_{12}$. Calculation of transverse shear modulus G_{23} and Poisson's ratio v_{23} was done by using semi-empirical Halpin-Tsai equations as described in [62]. These orthotropic material properties were the basis of simulating each type of the hybrid laminate. The stacking sequences of all six laminates discussed in Section 2.2.1 are listed in Table 2.3. By using an optical microscope (NIKON® SMZ 800N), the thickness of each individual layer in all laminates was measured to improve the accuracy of the FEM model.

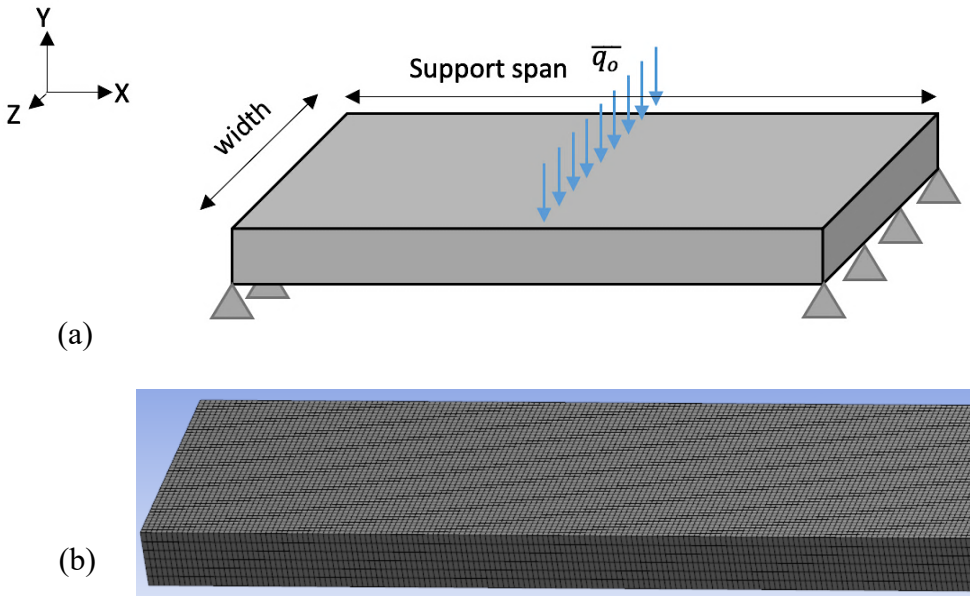

Fig. 2. 3 (a) Schematic of boundary conditions used for FEM modelling of bending specimen, (b) Mesh for the bending specimen

Following boundary conditions were used for the FEM modelling using ANSYS®: (i) along the simply supported edges any movement in the *z*-axis was restricted, (ii) the free edges were allowed to move freely along the *x* and *y*-axis, (iii) a uniformly distributed load ($\overline{q_o}$) was applied on the vertical mid-plane of the specimen in the negative *y*-axis as shown in Fig. 2.3a. Consequently, the total deformation of the specimen under the load, displacement along *x*-axis and mechanical strain maps were obtained by the FEM.

Table 2. 2 Mechanical properties of unidirectional carbon-epoxy and glass-epoxy laminates

Lamina material		Young's modulus [GPa]	Poisson's ratio	Shear modulus [GPa]	Strain at maximum load (%)
AC-UD	Carbon fiber reinforced epoxy composite	E_{11} = 121.58 E_{22}= 8.108 E_{33}= 8.108	v_{12}= 0.31 v_{13}= 0.31 v_{23}= 0.44	G_{12}= 4.124 G_{13}= 4.124 G_{23}= 2.798	1.376
AG-UD	Glass fiber reinforced epoxy composite	E_{11}= 40.736 E_{22}= 9.691 E_{33}= 9.691	v_{12}= 0.28 v_{13}= 0.28 v_{23}= 0.44	G_{12}= 3.445 G_{13}= 3.445 G_{23}= 3.334	3.312

Table 2. 3 Laminate stacking sequences (lamina sequence is in the positive z-direction)

Laminate	Lamina thickness [mm]	Total Thickness [mm]	Lamina materials	Lamina orientation (°)
1C-UD	(2.23/1.62/1.60/1.58/1.65/2.24)	10.92	[C/G/G/G/G/C]	$[0/0/0]_s$
2C-UD	(2.03/2.36/1.30/1.30/2.52/2.15)	11.65	[G/C/G/G/C/G]	$[0/0/0]_s$
3C-UD	(1.74/1.74/2.43/2.43/1.77/1.77)	11.87	[G/G/C/C/G/G]	$[0/0/0]_s$
13C-UD	(2.27/1.75/1.91/1.91/1.75/2.30)	11.88	[C/G/C/C/G/C]	$[0/0/0]_s$

3. RESULTS AND DISCUSSION

3.1 Flexural analysis of carbon/glass fiber reinforced hybrid composites

3-point bending test was used for the investigation of flexural properties of the hybrid laminates. The experimental results of three-point bending test are reported in Fig. 3.1. The figure shows stress versus strain curves of 1C-UD, 2C-UD, 3C-UD and 13C-UD laminates.

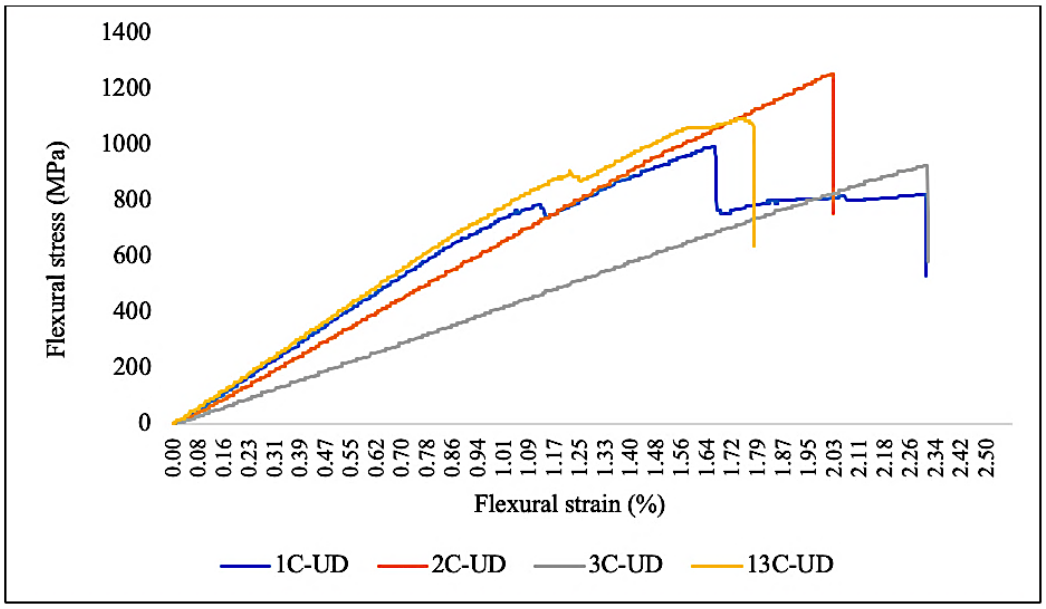

Fig. 3. 1 Flexural stress vs flexural strain curves for hybrid laminates

Using load cell data and real displacement of specimens, the stress and strain of specimens were calculated according to the ASTM standard (D790-03). The flexural response can be cataloged into three phases:

Phase 1: The relation between stresses and strain can be considered linear in the first part of the curve, and the material behavior is quasi-elastic. As shown in Fig. 3.1 this zone is widest for 3C-UD laminate (up to 2.32% strain corresponding to flexural strength of 928 MPa).

Phase 2: The relationship between stress and strain turns non-linear for the strain values of around 0.83%, 1.53% and 0.90% for 1C-UD, 2C-UD and 13C-UD laminates respectively. No such zone can be seen for 3C-UD laminate. However, in 1C-UD and 13C-UD laminates, the flexural modulus drops in a stepwise manner.

Phase 3: 2C-UD, 3C-UD & 13C-UD laminates show an instantaneous collapse corresponding to strain values of 2.03%, 2.32% and 1.77% respectively, and laminates behave like quasi-brittle materials. The collapse happens at a strain value of around 2.32% for 1C-UD laminate.

It is interesting to notice the staggered behavior exhibited by the curve of 1C-UD laminate. Its final failure occurred when several layers in the tensile and compressive zone suddenly and simultaneously broke. The average peak values for flexural strength, flexural modulus (in form of chord modulus) and flexural strain at maximum load for all laminates are shown in Fig. 3.2.

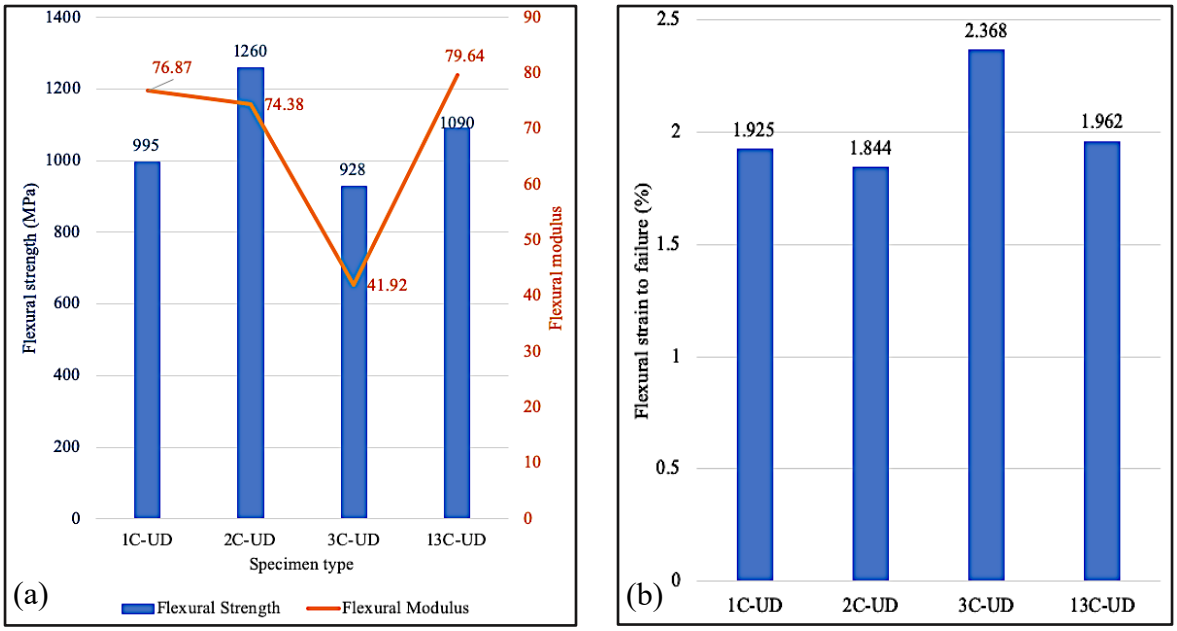

Fig. 3. 2 a) Flexural modulus and flexural strength of test specimens, (b) Flexural strain at maximum load

Flexural modulus values for the laminates of 1C-UD, 2C-UD, 3C-UD and 13C-UD were 76.87 GPa, 74.38 GPa, 41.92 GPa, and 79.64 GPa, respectively. Although the glass & carbon fiber content for 1C-UD, 2C-UD and 3C-UD samples are same, their flexural properties vary as a function of the laminate's stacking sequence. There is a decrease in flexural modulus from 1C-UD to 3C-UD and the lowest flexural modulus is exhibited by 3C-UD sample (41.92 GPa). As the carbon fiber layer moves towards the horizontal neutral axis of the laminates when we go from 1C-UD to 3C-UD laminate, a decrease in flexural modulus can be seen. The flexural strain at maximum load for 1C-UD and 2C-UD are comparable to each other. Highest flexural strain was exhibited by 3C-UD (2.36%). It is understood, the high ductility of glass fibers plays a significant role in increasing the strain value. The flexural strengths for laminates 1C-UD, 2C-UD, 3C-UD and 13C-UD laminates were measured as 995 MPa, 1260 MPa, 928 MPa, and

1090 MPa, respectively. Lowest flexural strength was observed in 3C-UD. This can be explained from the fact that 3C-UD had a sudden global failure in form of delamination along the horizontal mid-plane without any staggered failure as it had the presence of glass layers on the top and bottom faces. Very small difference in the values of flexural strengths and moduli of 1C-UD and 13C-UD laminates is observed. This stems from the presence of carbon fibers on the top and bottom surfaces in both laminate structures.

3.2 Damage initiation & propagation mechanisms

Failure in unidirectional composites is controlled mainly by the fiber breakages [63]. Due to the inherent profile of stresses under flexural loading conditions, the highest value of compression and tensile stresses are present at top and bottom layers of bending sample, respectively. Therefore, the initiation and growth of damage occurs from the surface layers of flexural specimen towards the inner layers. This susceptibility to failure at surface plies implies the importance of layup configuration under flexural loading conditions.

In 1C-UD laminate, staggered failure occurs, and the failure mechanism is complex as seen in Fig. 3.3. In the first phase, the micro-buckling of the compressive side occurred, as the top carbon layer failed to sustain the increasing pressure. The carbon fibers broke, thus transferring the load to the glass fibers beneath them which is obviously seen as buckling of glass layers in Fig. 3.4. This failure development corresponds to the initial stress drop in stress-strain curve of 1C-UD laminate i.e. at 1.12% flexural strain (Fig. 3.1). Similar buckling of top surface carbon layers was observed for thin fiber hybrid laminates under flexural loading conditions in a recent work by Tabrizi *et. al* [34].

In the second phase as seen in Fig. 3.3b, fibers at bottom layers showed abrupt rupture corresponding to the second stress drop in stress-strain curves. These fiber failures gave rise to interlaminar delamination which grew gradually in direction normal to the loading axis. The reason for this delamination can be related to the creation of free edges at ruptured fiber surfaces, continuation of transverse loading and out-of-plane shear stresses [64]. The rupture of carbon plies at the bottom and delamination of these brittle layers impeded at the interface between glass and carbon section which attributes to the third phase of failure development as seen in Fig 3.3c.

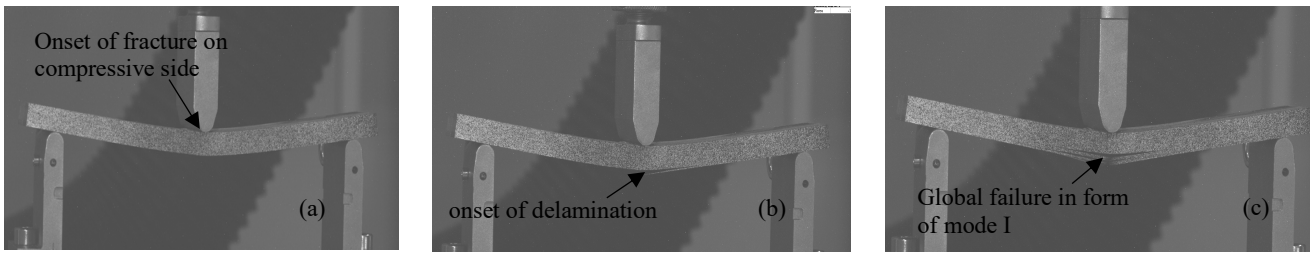

Fig. 3. 3 Damage evolution in 1C-UD

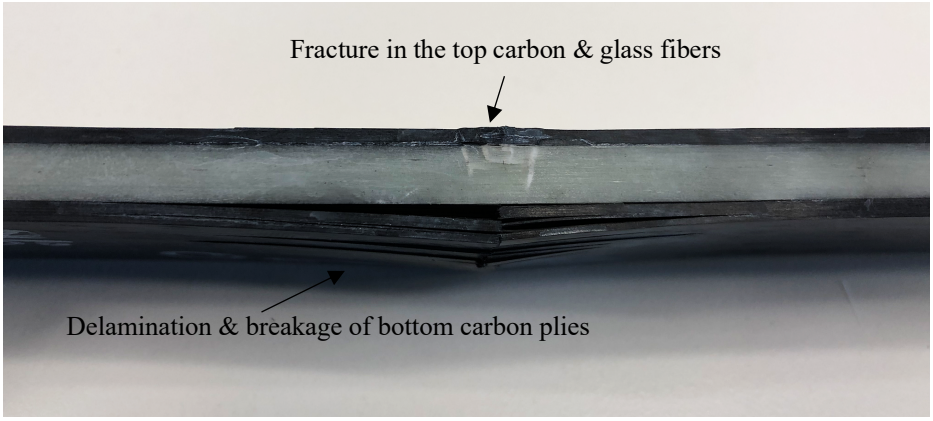

Fig. 3. 4 Side profile of 1C-UD laminate after failure

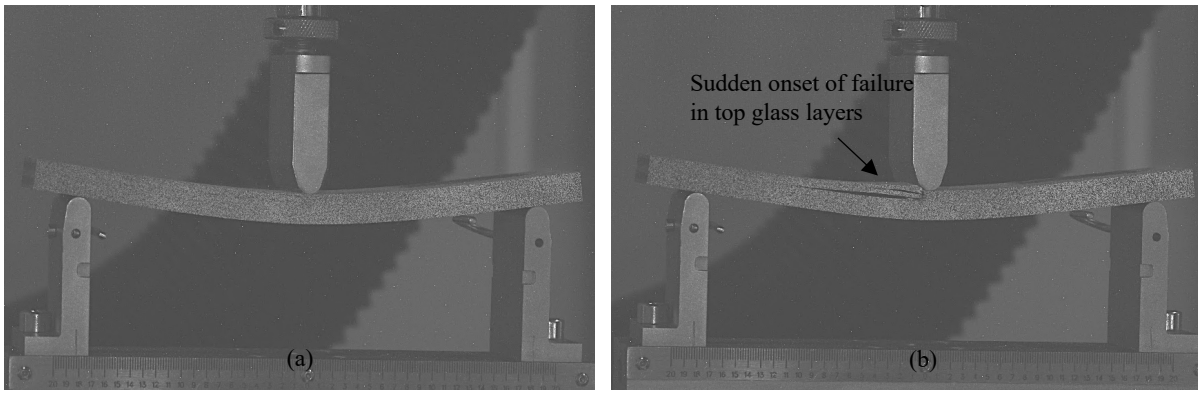

Fig. 3. 5 Damage evolution in 2C-UD a) before failure b) at global failure

In the 2C-UD laminate, glass layers are on the top and bottom faces of the specimen. The laminate sustains the applied load without failure until the strain value reached 2.03%. A buckling failure appeared at the top surface glass layers and continued to grow as a shear driven failure in carbon layers beneath them, as seen in Fig. 3.5. This shear driven failure then

developed as interlaminar delamination between the glass and carbon plies which is observed in Fig 3.5b. These observations are consistent with the results obtained for the same configuration in a previous study [34].

Chellappa *et al.* have stated that the delamination growth was an easy path for energy release for laminated fiber reinforced polymers compared to other transverse crack growth methods [65]. Therefore, the compressive transverse stress applied on this hybrid laminate resulted in a severe mode I delamination. It must be noted that the middle glass layers in 2C-UD sample presented damage development due to buckling. This exposure to compressive loads, despite the delamination failure between glass/carbon layers, can be related to an earlier delamination inside carbon layers (Fig. 3.6). Although the fracture occurrence in carbon layers distinguished the global failure of 2C-UD laminates, the structural integrity of the bottom layers remained uncompromised, as can be seen in Fig. 3.6.

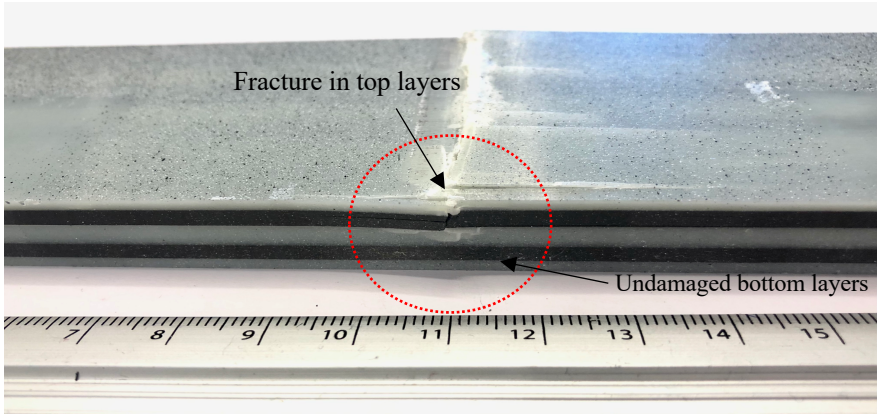

Fig. 3. 6 2C-UD laminate after the occurrence of global failure

The samples of 3C-UD and 13C-UD demonstrated a very fascinating damage mechanism as seen in Figs. 3.7 and 3.8. Both laminates contain carbon fibers along the horizontal midplane of the structures. The structure of 3C-UD laminate seems to appear like a sandwich structure with a carbon 'core' and glass 'faces'. Typically, in a sandwich laminate, the elastic modulus of the core is much less than that of the faces to resist extreme shear stress at the middle of the material thickness, and to resist bending deformation; but in 3C-UD laminate, the carbon core is more brittle than the faces. According to Paulo *et al.* [66], energy release rate due to mode II fracture of laminates directly relates to the elastic modulus of the material. Thus, higher elastic

modulus of carbon layers in the middle of the 3C-UD specimen made this region very susceptible to shear driven failure, i.e. slippage of carbon layer along the horizontal midplane due to interlaminar delamination, as this was a preferred energy release path. The onset of this shear driven failure was sudden, and the laminate separated into two halves exhibiting mode II delamination as seen in Fig. 3.7c. The stress-strain behavior of this laminate indicated a single stress-drop which corresponded to global failure of material, i.e. delamination growth along the specimen length. The interesting fact about this failure mode in 3C-UD laminate was the onset of damage from the left edge of specimen as seen in Fig. 3.7, while no visible macro damage was seen through the thickness at the loading point of the sample.

Similar behavior was observed in 13C-UD laminate, with complete separation of the laminate into two halves due to excessive shear stress accumulation along the horizontal midplane of the specimen. The first drop in the stress-strain curve of 13C-UD corresponded to the shear driven crack generation and its propagation through the thickness, until it reached the bottom glass layer, as indicated in Fig. 3.8a. Amaro *et al*. [66] found that the presence of defect near/at mid thickness of the laminate resulted in a variation of shear stress profiles; therefore, reducing the maximum load level for unstable delamination growth. Similarly, as the load was constantly being applied to 13C-UD sample, the onset of global failure in form of lengthwise interlaminar delamination became easier due to the presence of an early damage near the mid thickness plane. This unstable delamination growth at mid-plane corresponded to the final drop in the stress-strain curve of 13C-UD (Fig. 3.1).

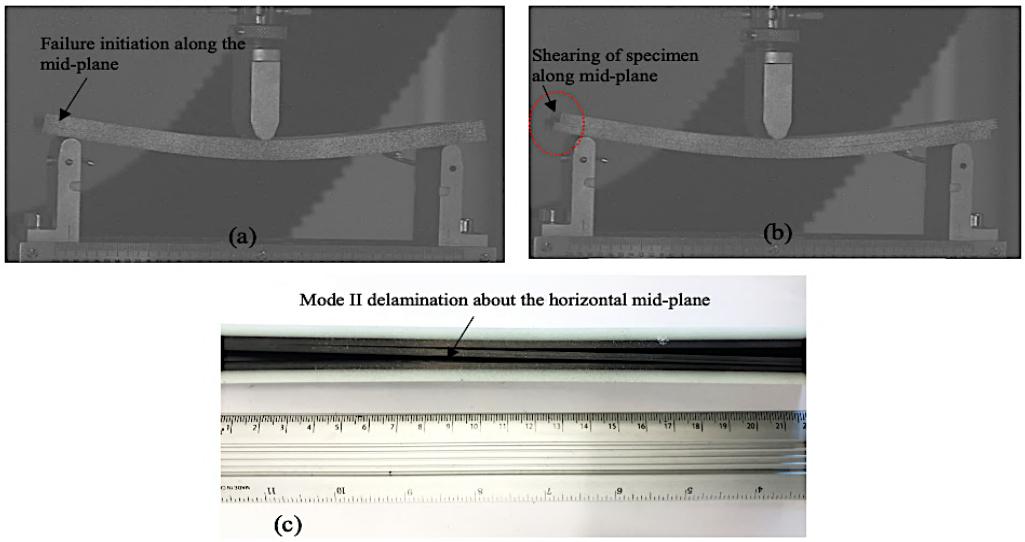

Fig. 3. 7 Global failure of 3C-UD laminate (a) Failure initiation, (b) Onset of interlaminar delamination along horizontal midplane, (c) Mode II delamination

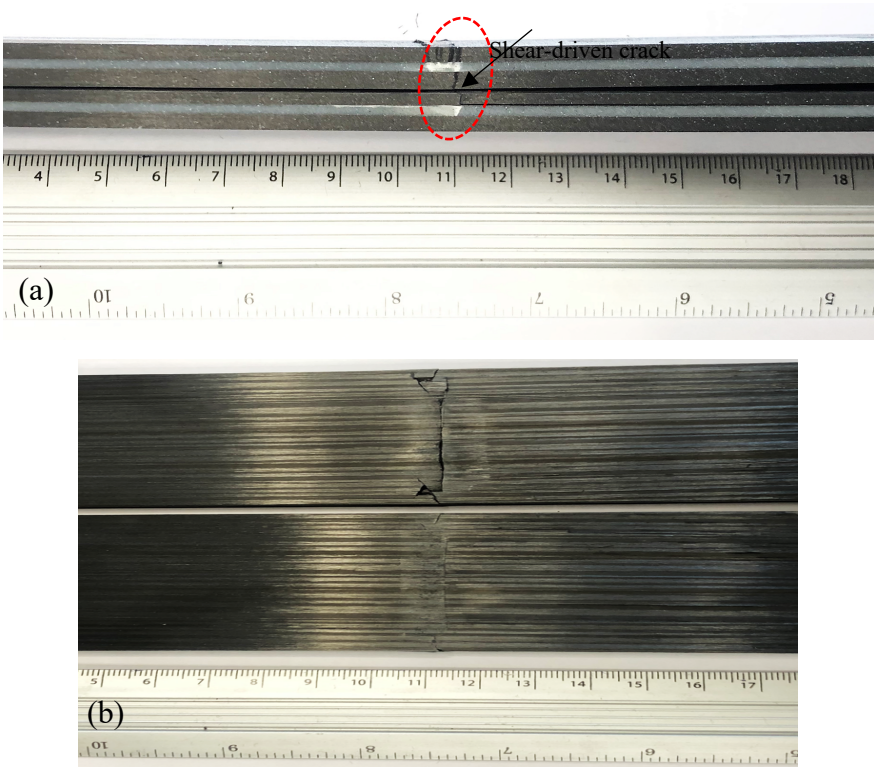

Fig. 3. 8 Splitting along horizontal midplane in 13C-UD specimen (a) side profile of the laminate and (b) global failure in form of separation of the laminate along horizontal neutral axis

3.3 Analysis of full-field strain and full-field displacement by using DIC technique

To apply the DIC technique for samples under flexural loading conditions, the stress level for the investigation was set to the value of 99% of the failure load. This normalization provided a benchmark for comparison of different laminates at the same lifetime, thus discarding possible errors due to experimental conditions. The DIC region of interest for all samples was confined to the area underneath the loading tip as the major strain changes are happening here. Fig. 3.9 shows the locations of the virtual strain gages chosen along the lengthwise direction of each specimen for DIC. Line 2 is at the horizontal midplane, and lines 1 and 3 are symmetric about line 2. The length of lines 1,2 and 3 i.e. gage length is equal to the total specimen length under examination.

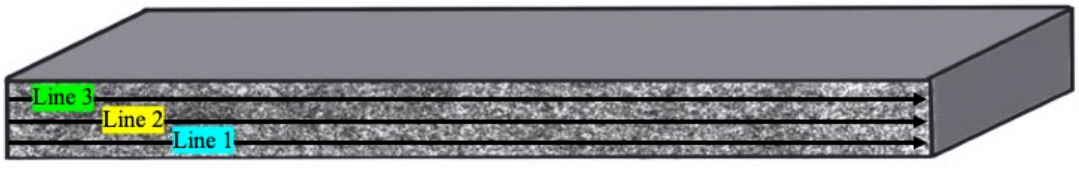

Fig. 3. 9 Location of virtual strain gages

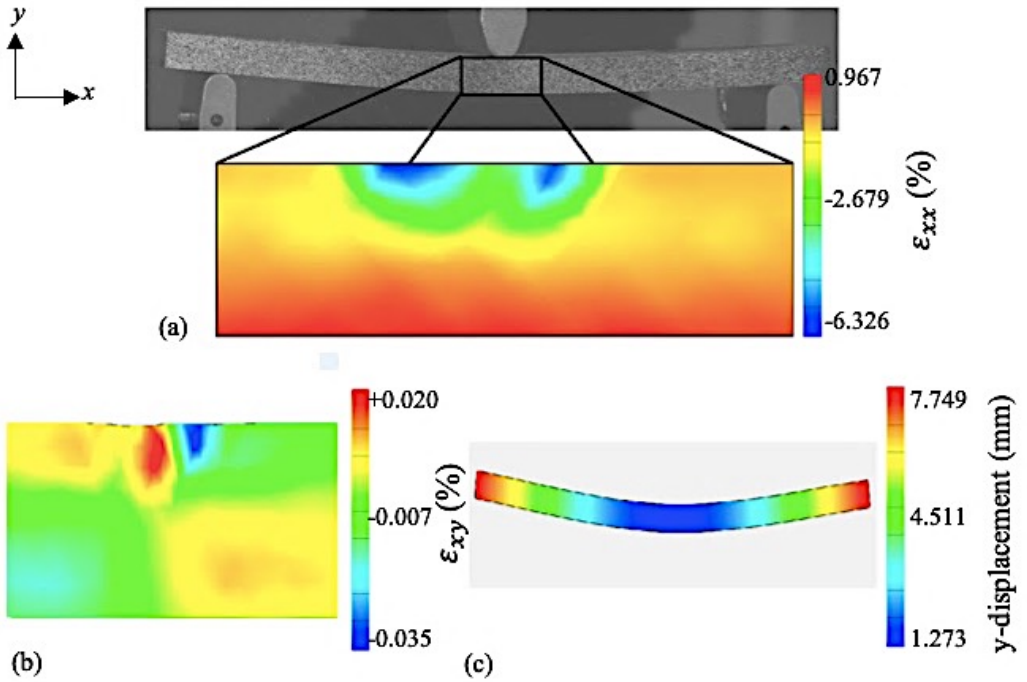

Fig. 3. 10 (a) Longitudinal strain (ε_{xx}), (b) shear strain field (ε_{xy}), (c) Displacement field for 1C-UD at 99% of failure load

Fig. 3.10 shows the computed full field longitudinal strain, shear strain and displacement distribution at 99% of the failure load along the gage length. As evident from the figure 3.10a, the highest strain region was distributed near the lower half of the specimen right before the occurrence of the global failure. The tensile strain in the lower carbon layers was nearly 15% more than the compressive strain present in the upper carbon layers. Whereas, a high compressive strain (≈-6.326%) can be seen below the loading nose. This is the point where onset of compressive fracture occurred (Fig. 3.3a). Simultaneously, just beneath the loading nose, opposite shear strain values existed in symmetry about the vertical midplane of the specimen (Fig. 3.10b). This concentration of shear strain variation through the thickness implies that the initial failure happens due to buckling at the top surface of the laminate. The opposite shear strains also imply the tendency of plies at top left side to slip onto the layers at top-right and vice versa. These observations revealed the complicated stress states through the thickness direction for 1C-UD laminate. Fig. 3.10c shows the displacement in y-direction i.e. parallel to the loading plane. Symmetry existed about the vertical midplane of the specimen, thus proving

that the load was applied properly to the middle of the specimen during testing. At 99% of the failure load, the average displacement in the y-direction was computed by DIC to be +4.407 mm.

Fig. 3.11 show the longitudinal strain (ε_{xx}) at 25% and 99% of the failure load for lines 1,2 and 3. The selection of 25% and 99% of failure load allowed to have a well-defined comparison between the profile of ε_{xx} at the beginning and end of the bending test on the top, middle and bottom of the specimen.

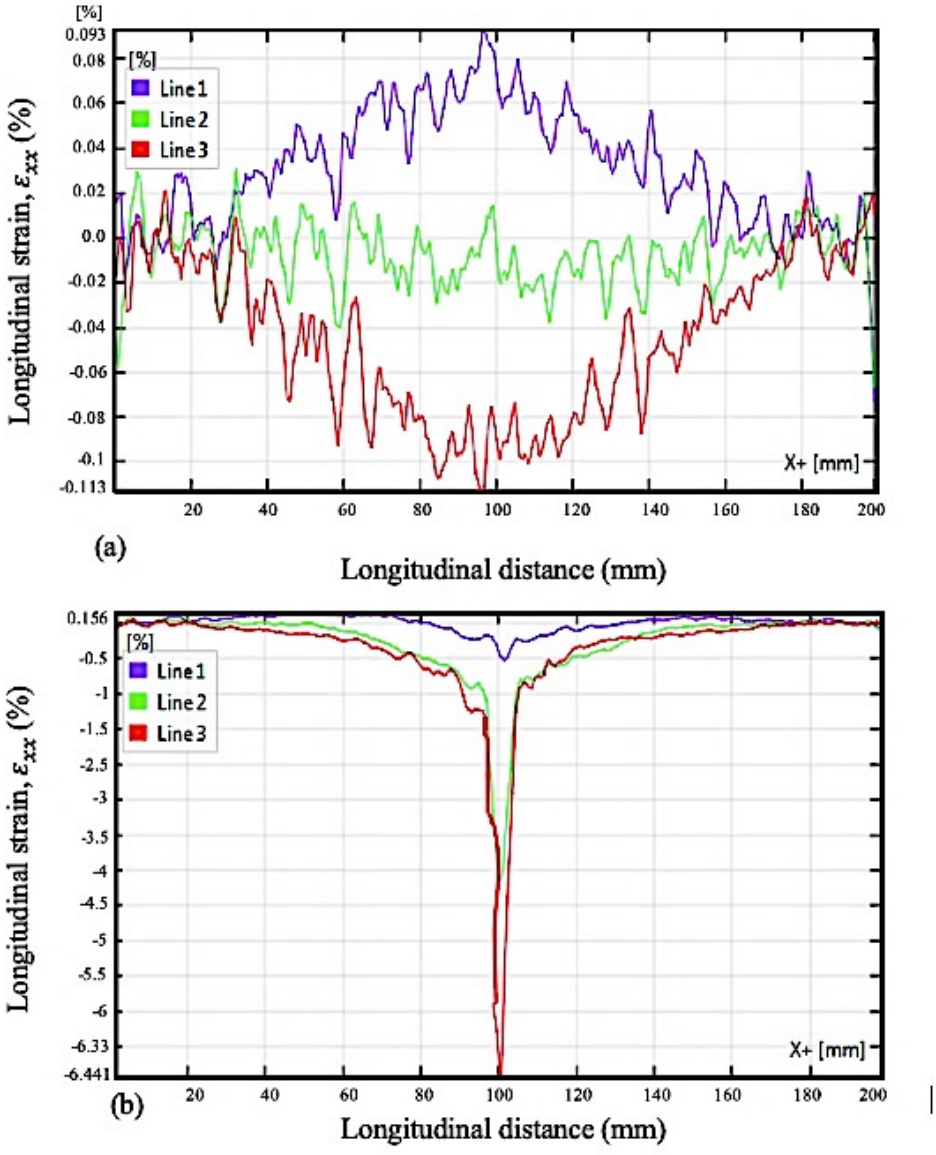

Fig. 3. 11 Longitudinal strain of 1C-UD laminate at: (a) 25% and, (b) 99% of failure load for lines 1,2 and 3

Fig. 3.11 shows the longitudinal strain (ε_{xx}) evolution along the gage length of the virtual strain gages. Line 1, 2 and 3 represent the bottom, middle and top of the specimen respectively. Line 1 showed a maximum of $\varepsilon_{xx} \approx 0.093$ % compared to $\varepsilon_{xx} \approx 0$ % for Line 2, and $\varepsilon_{xx} \approx$ -0.113 % for line 3 at 25% of the failure load. The strain value in the middle of the specimen was negligible at this stage and fluctuated from +0.03 % to -0.04 %. However, the highest strain region was distributed near the bottom of the specimen, which was under tension. But, when the loading force nearly reached the peak value during testing, a huge amount of compressive strain ($\varepsilon_{xx} \approx$ -6.441 %) was seen in the top part of the specimen. This strain concentration introduced the damage in 1C-UD laminate.

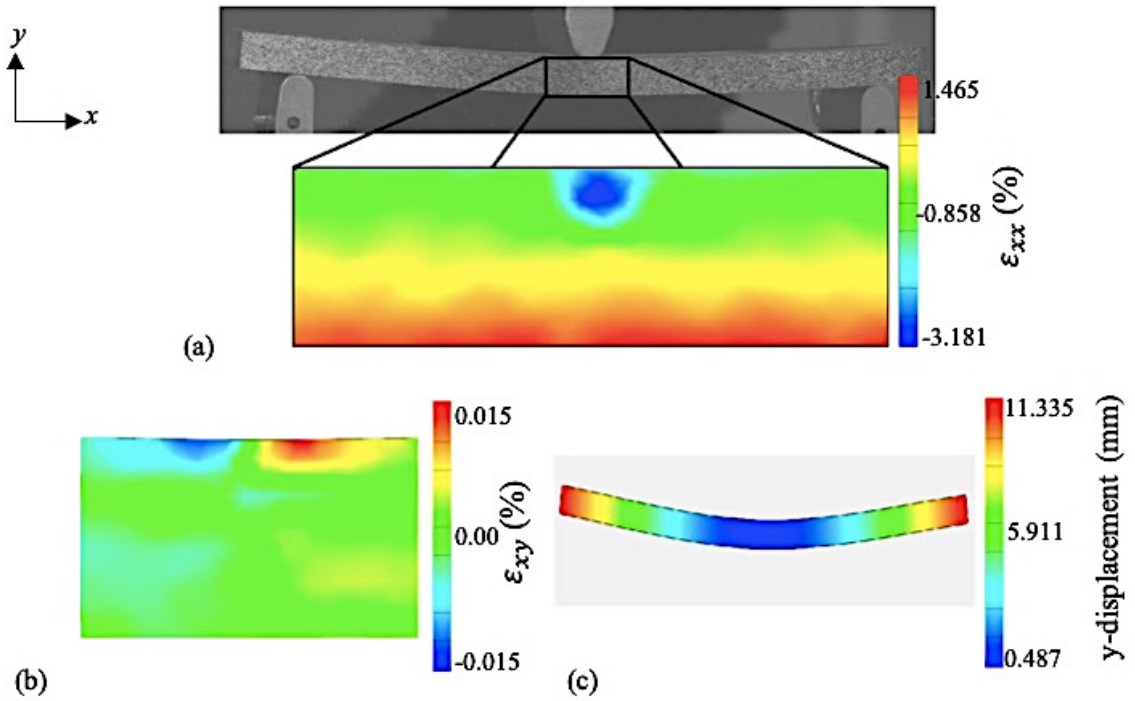

Fig. 3. 12 (a) Longitudinal strain (ε_{xx}), (b) shear strain field (ε_{xy}), (c) Displacement field for 2C-UD at 99% of failure load

Fig. 3.12 exhibits the longitudinal strain, shear strain and displacement field for 2C-UD laminate at 99% of the failure load. As seen in Fig. 3.12a, a compressive strain of $\varepsilon_{xx} \approx$ -3.181% is present underneath the loading nose describing the reason for sudden stress drop in the stress-strain curve of 2C-UD laminate. This high strain area corresponded to the region of fracture on the top surface shown in Fig. 3.5b, and the concentration of compressive strain finally culminated in the buckling failure of top glass layers of the laminate. Similarly, Fig. 3.12b shows the presence of symmetrical shear strains at the top layers which cause shear-driven

fracture in the middle of top layers of the specimen. However, there was almost zero shear strain elsewhere, which justifies the non-existence of damage in the bottom layers as can be seen in Fig. 3.6. This laminate sustained more bending deformation before the occurrence of global failure due to the presence of ductile glass layers on the top and bottom face. Fig. 3.12c demonstrates that the highest displacement in the direction parallel to the loading axis was present at the free ends (11.335 mm), however, an average y-displacement of +5.267 mm was observed in 2C-UD laminate at 99% of the failure load.

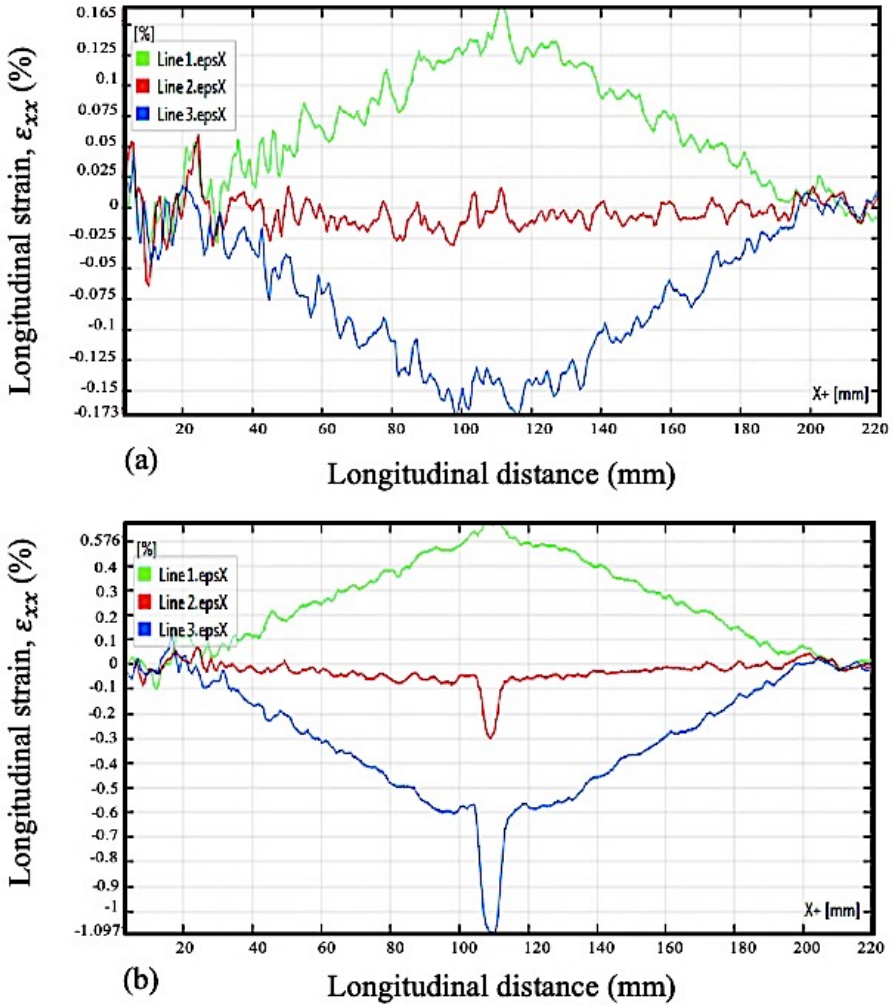

Fig. 3. 13 Longitudinal strain of 2C-UD laminate at: (a) 25% and, (b) 99% of failure load for lines 1,2 and 3

Fig. 3.13 shows the ε_{xx} profiles against the gage length of the virtual strain gages. Line 1, 2 and 3 represent the bottom, middle and top of the specimen, respectively. The longitudinal strain profile of 2C-UD resembles with that of 1C-UD's, with $\varepsilon_{xx} \approx 0$ along the horizontal mid-plane

of the specimen. Line 1 shows a maximum value of $\varepsilon_{xx} \approx +0.165$ (at 25% of the failure load), almost 2 times the value of ε_{xx} of 1C-UD for the corresponding line due to the replacement of carbon fibers in 1C-UD with glass fibers in 2C-UD laminate. However, at 99% of the failure load, a sharp peak was seen for Line 3 corresponding to the compressive strain value of $\varepsilon_{xx} \approx$ -1.097 % at the top layers. Excessive strain concentration in the middle of specimen instigated a sudden failure due to the buckling in the sample of 2C-UD.

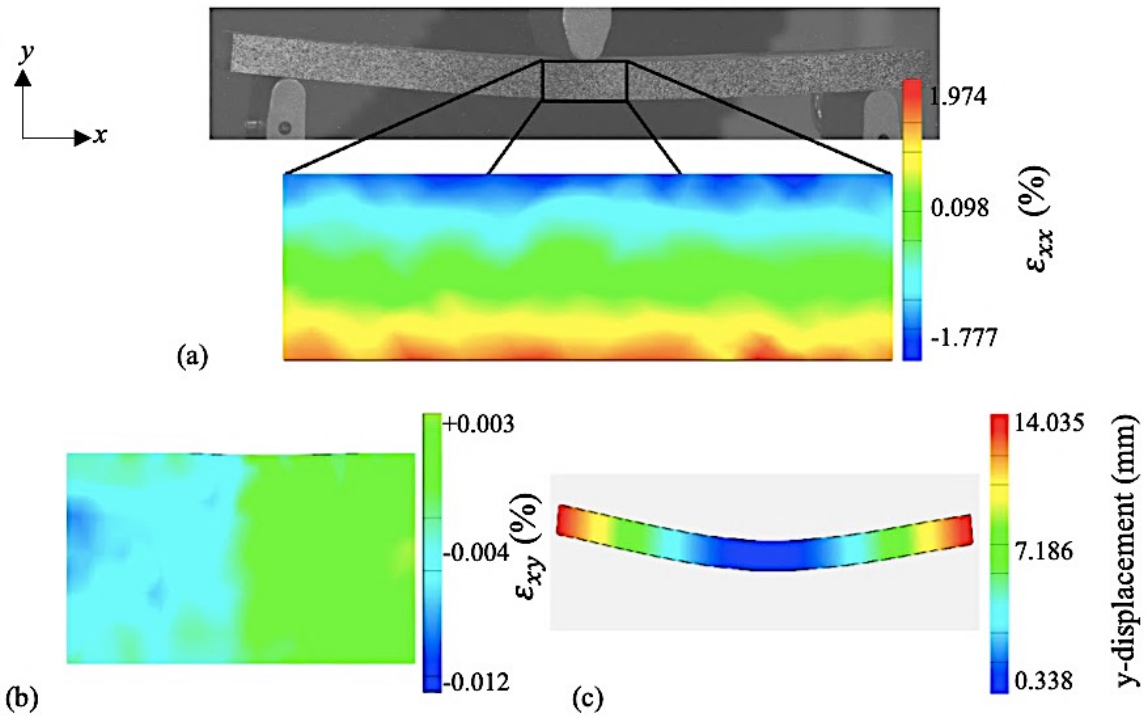

Fig. 3. 14 (a) Longitudinal strain (ε_{xx}), (b) shear strain field (ε_{xy}), (c) Displacement field for 3C-UD at 99% of failure load

Fig. 3.14 represents the longitudinal strain, shear strain and displacement fields for the 3C-UD laminate. The longitudinal strain is symmetric about the horizontal midplane of the specimen as observed in Fig. 3.14a. The area covered by both the tensile strain (bottom) and compressive strain (top) was comparable to each other. A compressive strain of -1.777 % at the top glass layers gradually became zero towards the mid-plane of the specimen. A tensile strain of +1.974% was present in the lowermost glass layers. The presence of opposite strains at the top and bottom layer triggered global failure owing to shear-driven delamination in the 3C-UD laminate. The damage initiation happened at the left side of the specimen and then moved along the horizontal midplane of the specimen. In Fig. 3.14b, there is a presence of compressive shear strain on the left side, which indicates the direction of propagation of failure from the left to

right side. In the laminate of 3C-UD, a high y-displacement with a maximum of 14.035 mm was detected because of the presence of more glass fibers on the top and bottom faces when compared to the laminates of 1C-UD and 2C-UD.

Fig. 3.15 shows the longitudinal strain values versus the specimen length for the three virtual strain gages created on the thickness surface of the laminate for 25% and 99% of the failure load. Lines 1, 2 and 3 represent the bottom, middle and top of the specimen, respectively.

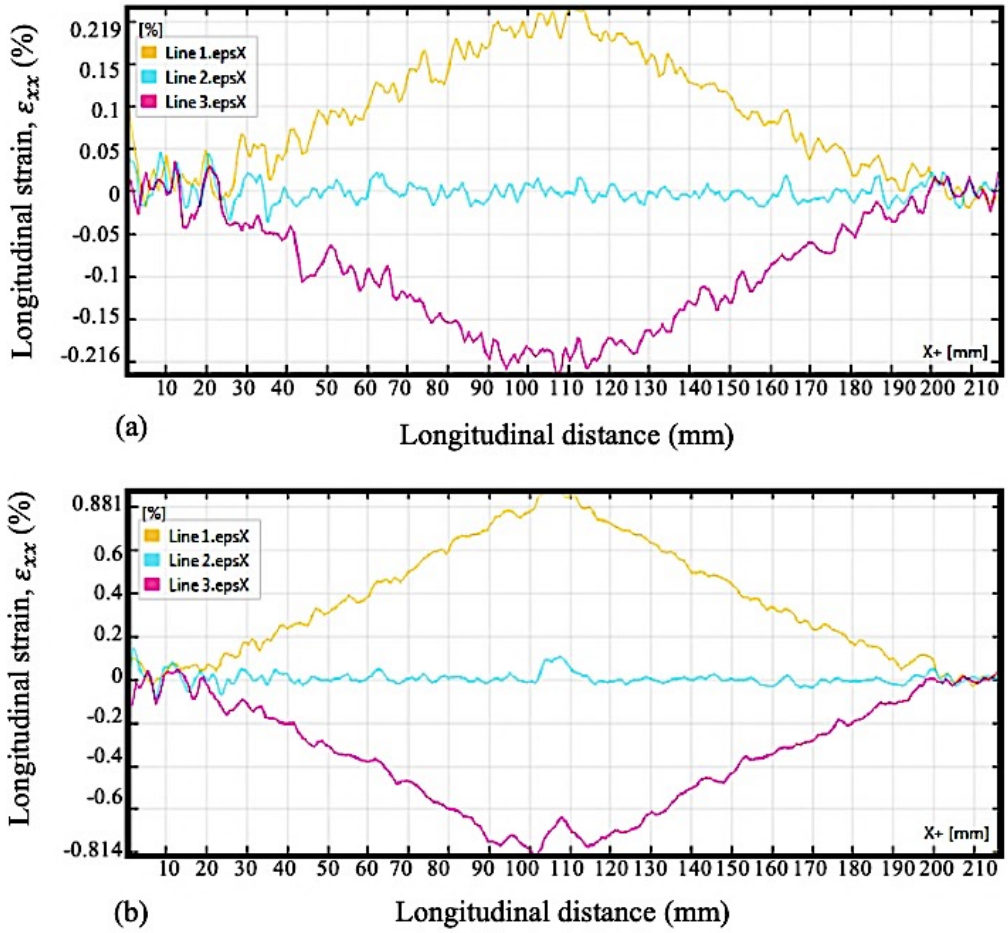

Fig. 3. 15 Longitudinal strain of 3C-UD laminate at: (a) 25% and, (b) 99% of failure load for lines 1,2 and 3

3C-UD laminate showed a fascinating behavior. Although the graph profiles did not change much for 25% and 99% of the failure load, a change of nearly 25% and 27% in the maximum values of tensile and compressive strain was observed, respectively. However, the longitudinal strain in the middle of the specimen remained close to 0 %. There was a separation of the laminate into two halves due to shear-driven interlaminar delamination (Fig. 3.7c). Line 1, 2,

and 3 showed a maximum of ε_{xx} ≈ 0.881%, ε_{xx} ≈ 0% and ε_{xx} ≈ -0.814% at 99% of the failure load respectively.

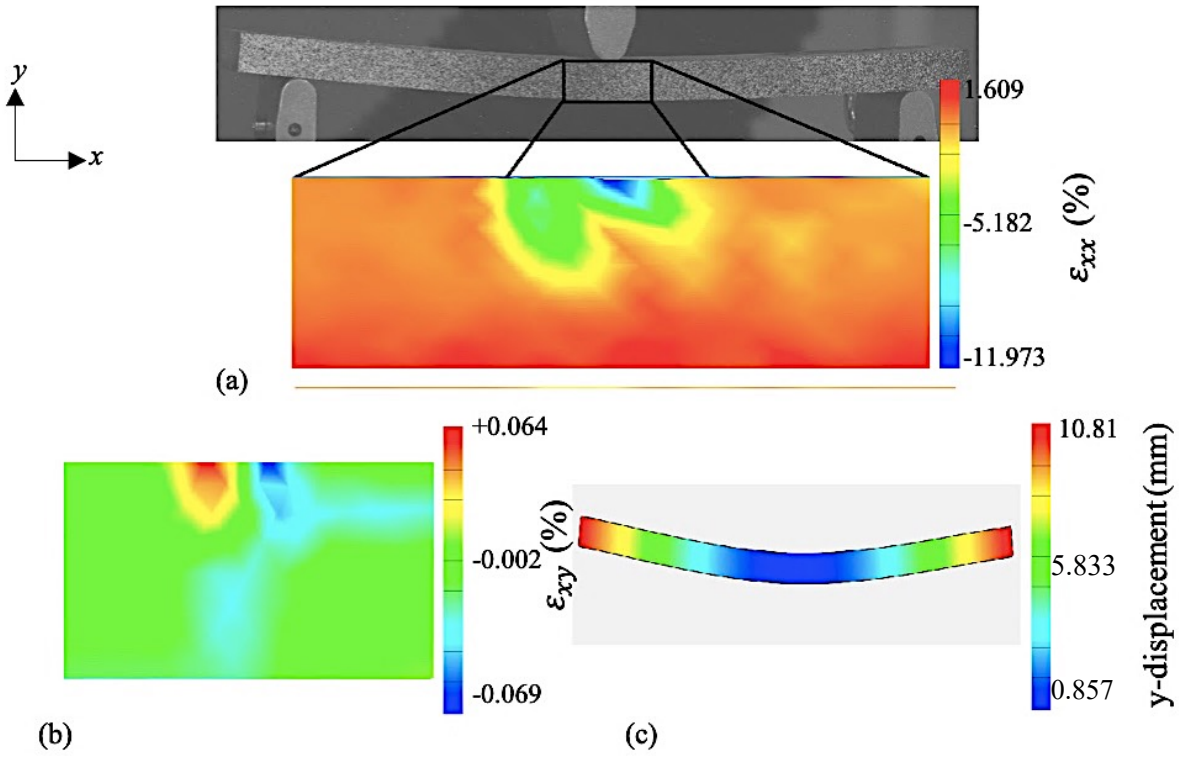

Fig. 3. 16 a) Longitudinal strain (ε_{xx}), (b) shear strain field (ε_{xy}), and (c) Displacement field for 13C-UD at 99% of failure load

Fig. 3.16 shows the longitudinal strain, shear strain and displacement fields for the 13C-UD laminate at 99% of the failure load. The global failure of 13C-UD was characterized by the shear-driven interlaminar delamination along the horizontal neutral axis of the specimen. Fig. 3.16a exhibits the map for longitudinal strain. It can be readily noticed that the area and value of tensile strain (+1.609 %) was much greater compared to the area and value of the compressive strain (-11.973 %) just underneath the loading nose. The high concentration of this compressive strain led to the fracture of the top carbon layers (Fig. 3.16b). As discussed in the previous section, 13C-UD separated in two halves upon the onset of global failure. A shear strain driven crack was observed in the middle of the specimen in Fig. 3.8a. This crack in the middle was generated by the compressive shear strain present in the middle of Fig. 3.16b. It can be noticed that the shear strain was very small (≈ -0.002 %) in the area surrounding the crack, thus limiting the propagation of crack in neighboring areas. As 1C-UD and 13C-UD laminates

both contain carbon layers on the top and bottom faces, so their damage mechanisms and flexural behaviors are comparable to each other. A maximum displacement of +10.81 mm in the y-direction was observed in 13C-UD laminate (Fig. 3.16c).

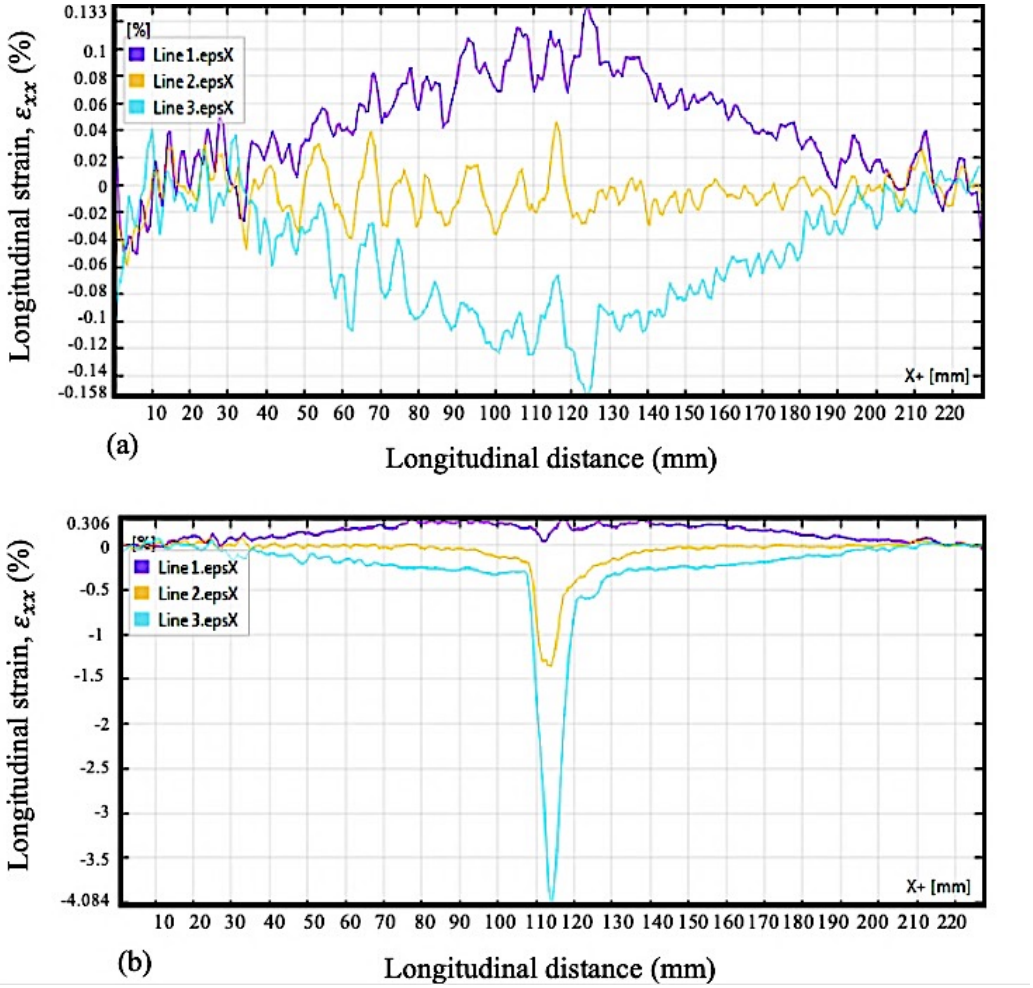

Fig. 3. 17 Longitudinal strain of 13C-UD laminate at: (a) 25% and, (b) 99% of failure load for lines 1,2 and 3

Fig. 3.17 shows the longitudinal strain profile as a function of specimen length for 13C-UD laminate. At 25% of the failure load there is a maximum longitudinal stress of $\varepsilon_{xx} \approx 0.133$ % and $\varepsilon_{xx} \approx 0.041$ % for Lines 1 and 2 representing the bottom and middle of the specimen respectively. However, a generation of compressive stress of $\varepsilon_{xx} \approx$ -0.158 % was seen at the top of the specimen. The profile completely changed near the failure load of the specimen under testing as shown in Fig. 3.17b. There is a stark peak for Line 3, reaching values of $\varepsilon_{xx} \approx$ -4.084% at the top-most layer of the specimen. This high compressive strain created a crack along the width of the specimen as seen in Fig. 3.8b. The value of ε_{xx} for Line 1 does not change

much along the length of the specimen at 99% of the failure load. There was a simultaneous generation of a long crack, and shear-driven delamination at this loading value as evident from both Fig. 3.17a and Fig. 3.17b.

3.4 Fracture surface analysis of carbon/glass fiber reinforced hybrid composites

The fracture surface characterization for all laminates was carried out by using optical microscopy and SEM. Fig. 3.18 represents the optical micrographs of the fracture surfaces for all laminates. The damage initiation and propagation mechanisms have been discussed in detail in Section 3.2. These micrographs are a continuation of the former discussion on damage modes. The failure onset in 1C-UD laminate was staggered, with the global failure manifestation in the form of tensile delamination of lower carbon layers and kinking of top carbon layers. The upper carbon layer exhibited a compressive failure due to the application of load on the top surface of the specimen in Fig. 3.18a. Although the compressive strain concentration caused buckling in the top surfaces of both 1C-UD and 2C-UD, the fracture surfaces were quite different from each other as seen in Fig. 3.18(a-b).

In 2C-UD, glass fibers are present on the top and bottom faces of the laminate. Sudden compressive failure in the form of buckling happened on the top surface, which can be clearly seen as the brushing of glass fibers in Fig. 3.18b. The damage modes in 3C-UD and 13C-UD were similar to each other as evident from Fig. 3.18c and Fig 3.18e, as both damage surfaces are alike. Both of these laminates failed due to the shear-driven interlaminar delamination along the horizontal midplane of the specimens. However, fracture on the top surface underneath the loading nose was observed in all the specimens, with varying intensities. This is due to the impact of the loading nose during the execution of bending test, and this fracture was most prominent in 2C-UD, and less noticeable in the 3C-UD laminate. Fig 3.18e shows one of the separated halves of 13C-UD laminate after the global failure. A clean delamination due to slippage of carbon layers against each other along the horizontal neutral axis was observed. 13C-UD laminate also sustained fracture on the top carbon layers which can be seen in Fig. 3.18f in the form of buckling.

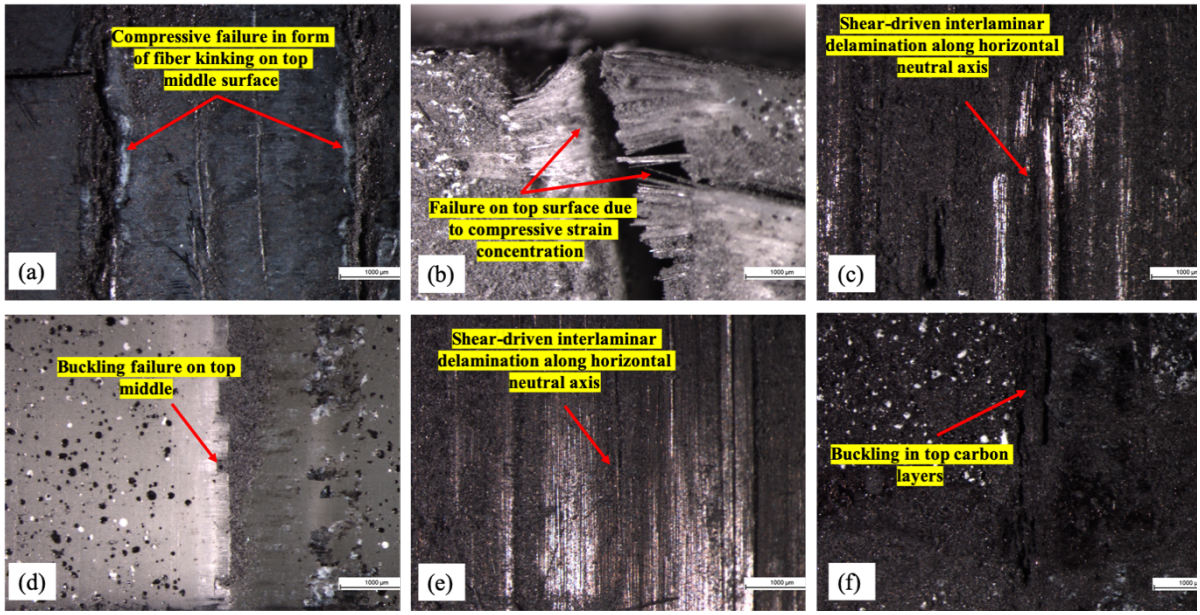

Fig. 3. 18 Stereo Optical Microscopy images of fractured surfaces: (a) Top surface of 1C-UD laminate, (b) Buckling failure in 2C-UD laminate, (c) Separated half of 3C-UD laminate (d) Kink band formation on top glass layers in 3C-UD laminate, (e) Separated half of 13C-UD laminate due to shear-driven interlaminar delamination, (f) Buckling in top carbon layers in 13C-UD

Fig. 3.19 shows SEM images of the fractured surfaces for the laminates. Matrix cracking was detected on the surface of top carbon layers in 1C-UD laminate due to high compressive strain concentration underneath the loading nose as shown in Fig. 3.19(a-b). Due to crazing of the matrix, several voids also appeared on the fracture surface. Start of another cracking event in the form of a blister can be seen in Fig. 3.19b. Furthermore, Fig. 3.19(c-d) displays the fractured surface of 2C-UD laminate. A sudden onset of compressive failure occurred in the laminate of 2C-UD in the top glass layers. The failure in this laminate was manifested in the form of buckling and matrix cracking as seen in Fig. 3.19(c-d). Fig. 3.19(e-g) shows the SEM micrographs of the fracture surfaces of 3C-UD and 13C-UD laminates. Herein, both laminates manifested global failure in the form of interlaminar delamination along the horizontal neutral axis of the specimen. Brushing and breakage of carbon fibers has occurred in 3C-UD as observed in Fig. 3.19e. Fig. 3.19f provides a better visualization of delamination of the fibers from the laminate surface. Due to breakage of fibers, carbon particles can be seen in the SEM images due to the inherent brittleness of carbon fibers. No such carbon powder formation was detected for glass fibers in any of the laminates. Fig. 3.19g and Fig. 3.19h shows SEM images for one of the separated halves shown previously in Fig. 3.8b of 13C-UD laminate.

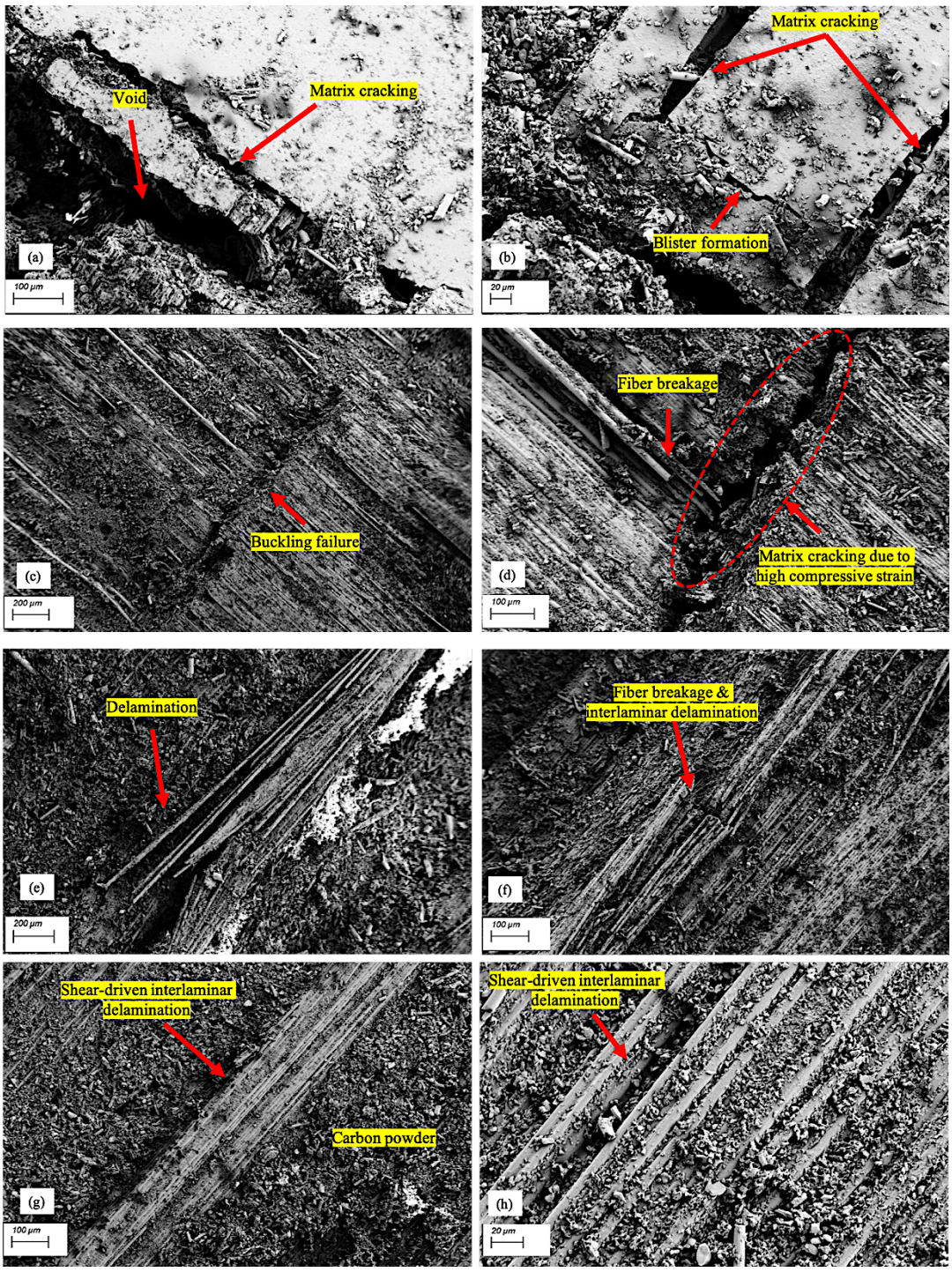

Fig. 3. 19 SEM images of fractured surfaces: (a) Matrix cracking and void formation in top carbon layers of 1C-UD laminate and (b) Onset of matrix crazing in form of a blister formation in top carbon layers of 1C-UD laminate, (c) Onset of kink band in the top glass layer of 2C-UD laminate and (d) Buckling failure on the top glass layer of 2C-UD laminate, (e) Shear-driven delamination in 3C-UD laminate and (f) Shear-driven fiber breakage and interlaminar delamination of 3C-UD laminate, (g-h) Shear-driven interlaminar delamination along the horizontal neutral axis of 13C-UD laminate

It is interesting to notice that the fiber breakage was not a prevalent form of damage in both 3C-UD and 13C-UD laminates, unlike the other two laminates as seen in Fig. 3.19(e-h). To conclude, the absence of matrix cracking and void formation in 3C-UD and 13C-UD can make these materials safer during their lifecycle under normal working conditions when compared to the structures of 1C-UD and 2C-UD laminates.

3.5 FEM results

The main goal of this part is to calculate the longitudinal displacements, longitudinal strain and shear strains exhibited by the laminates under flexural loading conditions using FEM. For this purpose, a commercial FEA tool (ANSYS®) has been used with a custom code using solid elements for meshing of the specimen geometry. FEM is repeated for each laminate according to the method described in Section 3.2.

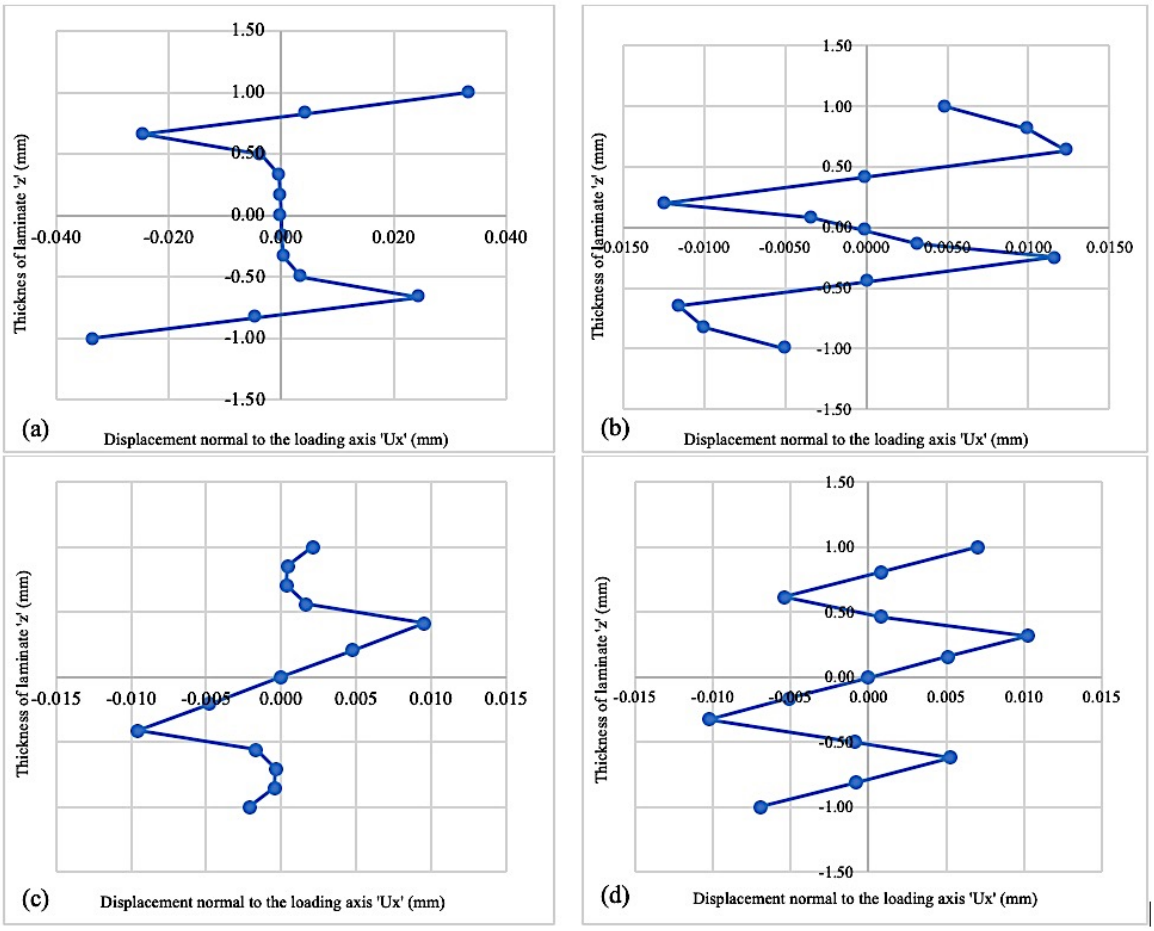

Fig. 3. 20 Plots of displacement in the x-direction (U_x) versus thickness (z) of the specimen (a)1C-UD, (b) 2C-UD, (c) 3C-UD, and (d) 13C-UD

Fig. 3.20 shows the variation of U_x (displacement in direction normal to the loading axis) as a function of z (specimen thickness) for a prescribed value of x. For the simplification of the study, only the nodes on the free edges of the specimen were chosen and same amount of pressure (3 MPa) was used for the FEM analysis. *Y-axis* has been normalized to make the comparison easier. An analogy can be established between the two layup types and the laminates, i.e. (i) a 3-layer sandwich-like laminate, and (ii) a 5-layer laminate. As explained in earlier sections, 1C-UD laminate contains carbon layers on the top and bottom and thus an analogy with a 3-layer sandwich structure can be made. A similar correlation can be established for 3C-UD laminate as it contains carbon layer sandwiched between glass layers. 2C-UD and 13C-UD laminates can be classified as 5-layer hybrid laminates.

The plot for 1C-UD laminate ranged from longitudinal strain values of -0.0334 % and 0.03343 %. This plot is comparable to the plot for a 3-layer sandwich structure as the zigzag graph changed dramatically only three times as shown in Fig. 3.20a. Similar plot of the zigzag function for a laminate with the same configuration was seen in [34]. The strain values for 2C-UD laminate ranged from -0.0050 % to 0.0049%. It can be seen in Fig. 3.20b that the slope of the plot changed abruptly only five times, thus validating the treatment of 2C-UD laminate as a five-layer hybrid structure. The strain values for 3C-UD ranged from -0.0021% to 0.0021%. Upon approximation, it was seen that the slope of the plot for 3C-UD had three abrupt direction changes evident from Fig. 3.20c. Thus, 3C-UD behaved like a three-layer sandwich laminate with glass fiber faces and carbon fiber core. The behavior of 13C-UD was like a five-layer hybrid composite with carbon fiber on the faces, a carbon fiber core and glass fibers sandwiched between the faces and core. The longitudinal strain values ranged from -0.007% to 0.007% for 13C-UD.

Fig. 3.21 shows the plot of average displacement along the axis parallel to the loading axis as a function of different levels of loading i.e. 25%, 50%, 75% and 99% for all laminates. The average displacements along the axis parallel to loading direction at 99% of loading for 1C-UD, 2C-UD, 3C-UD and 13C-UD laminates were +4.807 mm, +4.812 mm, +5.718 mm and +5.227 mm respectively as computed by the FEM. A trend of 1C-UD < 2C-UD < 13C-UD < 3C-UD was seen for the displacement values. However, the values of average displacements computed with FEM software were found to be smaller than the actual displacement values

exhibited by the laminates during the bending tests by ~ 15.31% (average). This discrepancy can be explained by the fact that the FEM software considers a state of perfect interfacial bonding between the layers of the laminate, without taking into account the possible manufacturing faults like uneven thickness, voids and improper curing.

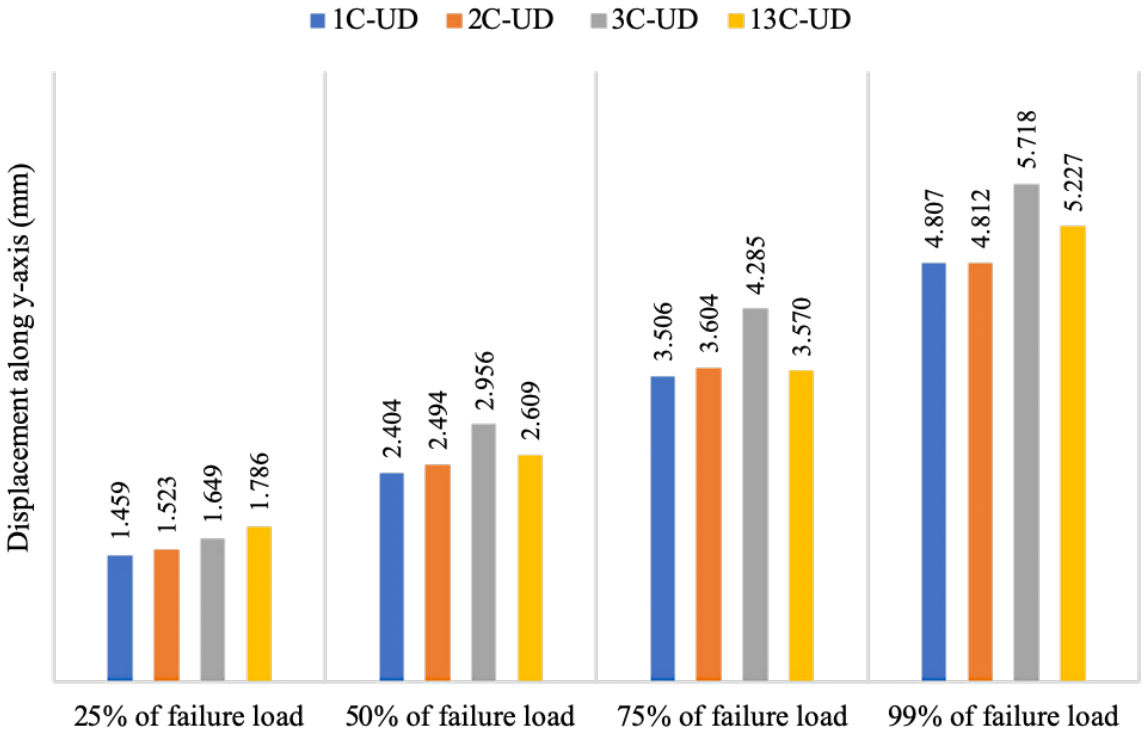

Fig. 3. 21 FEM results of average displacement (mm) along axis parallel to loading direction i.e. y-axis

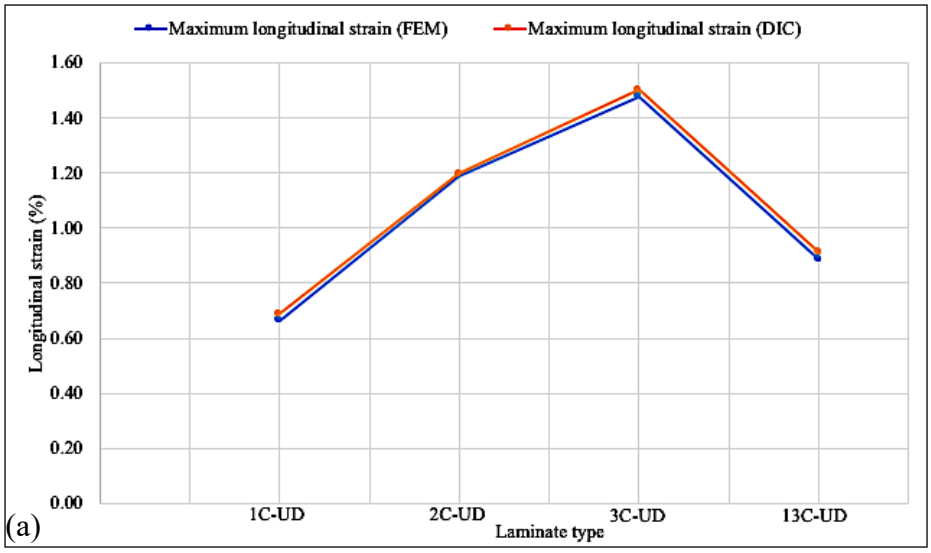

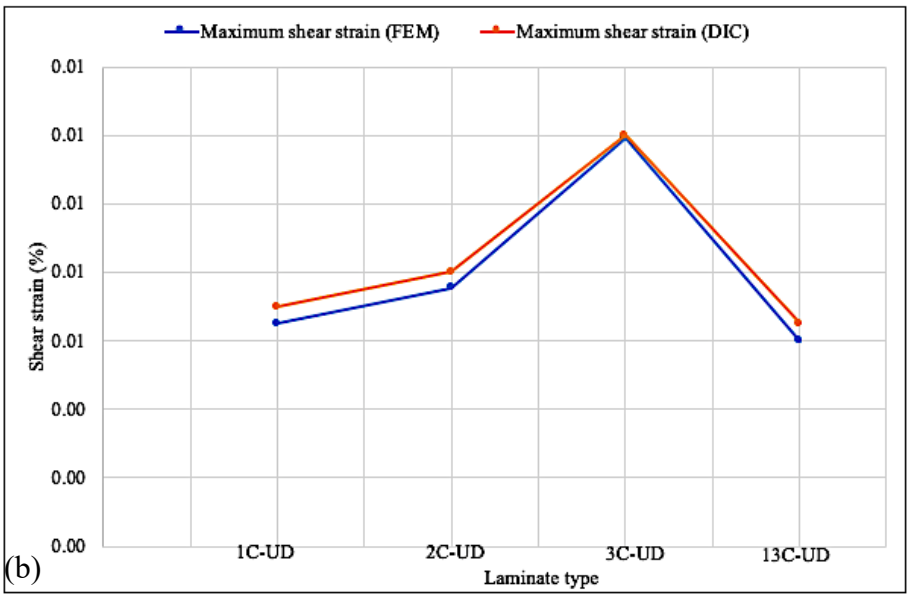

Fig. 3. 22 Comparison of FEM and DIC results for all laminates for (a) Longitudinal strain, (b) Shear strain

Fig. 3.22 shows the comparison between plots of longitudinal and shear strain values obtained from the experiments and FEM analysis. For simplification 75% of the failure load was selected for all laminates. An average error of ~ 1.79% was seen between the values obtained from the experiments and FEM. This can be explained by the fact that the FEM analysis software considers perfect interfacial bonding in the laminates and does not account for the manufacturing faults like voids and improper matrix curing.

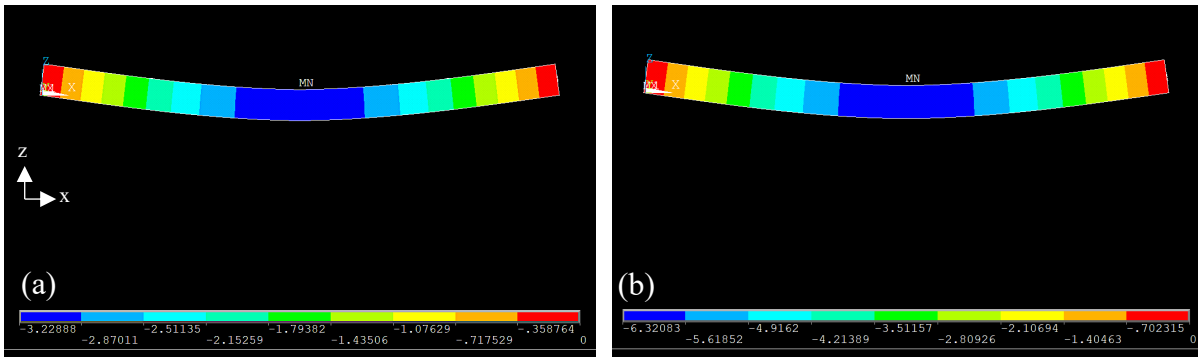

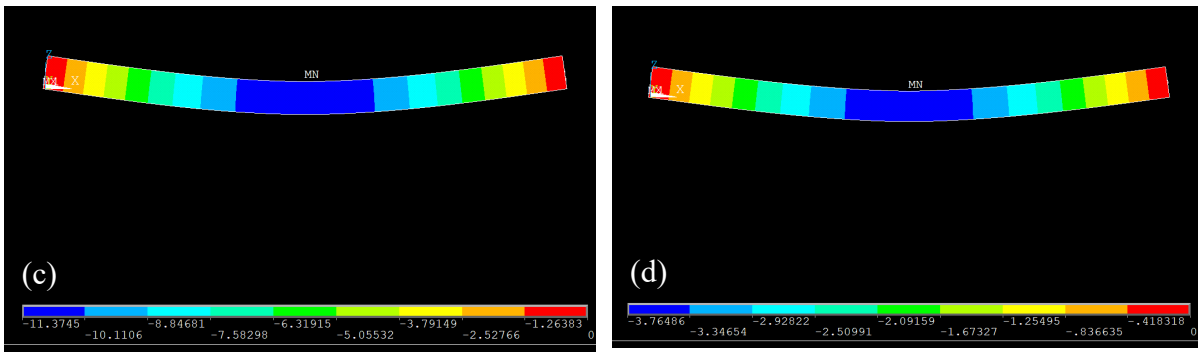

Fig. 3. 23 Maximum displacement along axis parallel to the loading direction (a) 1C-UD laminate, (b) 2C-UD laminate, (c) 3C-UD laminate, (d) 13C-UD laminate

Fig. 3.23 show the displacement along the axis parallel to the loading direction computed by FEM for all laminates at 75% of the failure loading. It can be noticed here that the largest displacement was shown by 3C-UD laminate i.e. 11.37 mm and the smallest displacement was observed for 1C-UD laminate i.e. 3.22 mm. The trend for maximum displacements i.e. 3C-UD > 2C-UD > 13C-UD > 1C-UD was consistent with the DIC results.

4. CONCLUSION

The influence of externally weak layers on the flexural response of carbon/glass fiber reinforced hybrid composites was evaluated by experimental and numerical approaches. In the experimental part of this thesis, the laminate samples were fabricated by hot-press technique in four different configurations. In each sample, 48 prepreg plies were utilized and their configurations were set to $(C_8/G_8/G_8)_s$, $(G_8/C_8/G_8)_s$, $(G_8/G_8/C_8)_s$, and $(C_8/G_8/C_8)_s$. Then, the mechanical performance of the prepared hybrid laminates was analyzed by applying 3-point bending tests. The results of flexural tests indicated that the highest flexural strength (1260 MPa) was exhibited by the laminate with the configuration of $(G_8/C_8/G_8)_s$, and the highest flexural modulus (79.64 GPa) was shown by the laminate with configuration of $(C_8/G_8/C_8)_s$. The relation between stress and strain was linear in the first part of the stress-strain curve for all the laminate and the material behavior was quasi-elastic. For 3C-UD laminate this zone was the widest, with a 2.32% strain corresponding to flexural strength of 928 MPa. The flexural strength for the laminates showed the trend as following:

2C-UD > 13C-UD > 1C-UD > 3C-UD

Although the laminates of 1C-UD, 2C-UD and 3C-UD had the same volume fraction of carbon and glass fibers, their flexural properties varied as a function of the laminate's stacking sequence. Flexural modulus values of the laminates 1C-UD, 2C-UD, 3C-UD and 13C-UD were 76.87 GPa, 74.38 GPa, 41.92 GPa, and 79.64 GPa, respectively; and the trend seen for flexural moduli is as below:

13C-UD > 1C-UD > 2C-UD > 3C-UD.

In addition, DIC technique was used to obtain full-field displacement and strain maps during the flexural test for all specimens. It was observed that the behavior of stress-strain curve was affected by the type of fibers present on the faces of the laminates. Presence of carbon fibers on the both the top and bottom faces caused staggered failure of the laminate, as shown by the stress-strain curve of 1C-UD and 13C-UD laminates. Presence of glass fibers on the top and bottom faces caused a sudden global failure of the laminate as seen for 2C-UD and 3C-UD laminates. The replacement of glass fiber layer along the horizontal midplane of 1C-UD laminate with carbon fibers (as in 13C-UD) had no significant effect on the of the flexural properties. In addition, the type of fibers present along the horizontal midplane of the laminate governed the mode of failure exhibited by the laminate. For example, both 3C-UD and 13C-

UD laminates had carbon fibers along the horizontal neutral axis, and both failed by shear-driven interlaminar delamination (mode II fracture). Furthermore, the longitudinal strain of the middle layers along the horizontal neutral axis of 2C-UD and 3C-UD laminates remained closer to 0% until the occurrence of global failure of the laminates, since the external glass layers in both laminates sustained the majority of the applied load resulting in higher strain values on the laminate's top and bottom surfaces.

If an indication of failure onset is needed, then carbon fibers should be placed on the faces as it will then cause a staggered failure, thus 1C-UD and 13C-UD configurations will be suitable. However, if the force (during the working conditions) being applied on a laminate does not exceed 15000 N during the lifetime, 3C-UD configuration will be the best one since it shows no detectable signs of damage before 20000N (that is when global failure in form of separation occurs).

Cross-sectional analysis of fractured specimens was done by optical microscopy and SEM. The optical analysis of fracture surfaces showed that the prevalent modes of failures in laminates were related to the formation of kink bands on top surfaces due to the impact of loading nose (in all laminates), and interlaminar delamination (in 1C-UD, 3C-UD and 13C-UD laminates). The SEM characterization validated the damage initiation behavior analysis of the laminates using DIC.

In the numerical part of the thesis, the Finite Element Method (FEM) was used to validate the experimental values of displacement and strains for all laminates. From the experimental and computational results, following conclusions can be deduced:

- The plot of displacement in the direction transverse to the loading axis at the free edges of the bending specimen versus the specimen thickness showed a zigzag behavior for all laminates.
- A trend of 1C-UD < 2C-UD < 13C-UD < 3C-UD was seen for the average displacements (computed by FEM) along the direction parallel to the loading axis.
- 1C-UD and 3C-UD laminates can be treated as three-layer sandwich structures, whereas 2C-UD and 13C-UD laminates can be treated as five-layer hybrid structures based on the information provided by the plot of displacement in direction normal to the loading axis versus the laminate thickness.

Table 3.1 summarizes the mechanical and cost performances of the produced hybrid laminates.

Table 3. 1 Summary of important properties of thick carbon/glass fiber reinforced hybrid composite laminates

Laminate type	1C-UD	2C-UD	3C-UD	13C-UD
Configuration	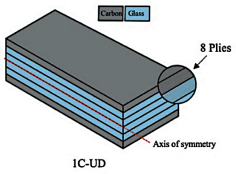	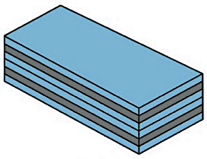	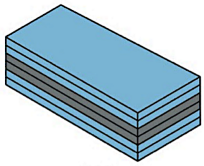	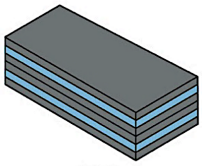
Flexural strength (MPa)	995	1260	928	1090
Flexural modulus (GPa)	76.87	74.38	41.92	79.64
Cost-to-performance ratio[+]	****	**	*	***
Maximum Longitudinal strain at 99% of failure load (%)	+0.967	+1.465	+1.974	+1.609
Maximum shear strain at 99% of failure load (%)	+0.020	+0.015	+0.003	+0.064
Maximum displacement at 99% of failure load (mm)	7.749	11.335	14.035	10.81
Prevalent mode of failure	Interlaminar Delamination on tensile side	Buckling failure on compressive side	Interlaminar delamination along horizontal neutral axis	Interlaminar delamination along horizontal neutral axis

[+] ****** = Best, *** = Good, ** = Average, * = Poor**

Future work

The research conducted in this thesis will expand the utilization of unidirectional carbon/glass fiber reinforced hybrid laminates. Similar investigation will also be feasible for fabric-based hybrid composites and prepreg-based cross ply and quasi-isotropic laminates. The process optimization of hot press technique can be carried out by using a range of process parameters especially by changing the pressing pressure. The stacking sequence might be further extended to produce more variations of the 48-layer thick hybrid composites. Additionally, comparison between the thick-section hybrid composites manufactured through the hot-press technique and resin transfer molding technique is also conceivable to study the effect of manufacturing technique on the mechanical properties of the laminate. Moreover, graphene reinforced carbon/glass fiber hybrid composites could be manufactured to understand the effect of graphene reinforcement on the composite's mechanical performance.

REFERENCES

[1] M. I. Daniel and O. Ishai, "Introduction," in *Engineering Mechanics of Composite Materials*, New York: Oxford University Press, Inc., 1994, pp. 3–11.

[2] R.-M. Wang, S.-R. Zheng, and Y. G. Zheng, "Introduction," in *Polymer Matrix Composites and Technology*, Cornwall, UK: Woodhead Publishing, 2011, pp. 1–5.

[3] P. K. Mallick, "Materials," in *Fiber-Reinforced Composites: Materials, Manufacturing, and Design, Second Edition, Revised and Expanded*, USA: Marcel Dekker, Inc., 1993, pp. 15–21.

[4] G. Staab, "Lamina Analysis," in *Laminar Composites 2nd Edition*, 2nd ed., Butterworth-Heinemann, 2015, pp. 37–38.

[5] Shindo A., "Carbon Fibers from Cellulose Fibers," *Appl. Polym. Symp.*, vol. 9, p. 271, 1969.

[6] K. K. Chawla, "Reinforcements," in *Composite Materials: Science and Engineering*, Springer, 2012, pp. 24–26.

[7] A. K. Asthana and N. V. R. Rao, "Applications of Fibre-glass Reinforced Plastics in Building and Construction Industry," in *Innovative Housing Practices*, Oxford: Elsevier, 1989, pp. 141–146.

[8] H. Nguyen, W. Zatar, and H. Mutsuyoshi, "Mechanical properties of hybrid polymer composites," in *Hybrid Polymer Composite Materials: Properties and Characterisation*, V. K. Thakur, M. K. Thakur, and A. Pappu, Eds. Woodhead Publishing, 2017, pp. 89–90.

[9] M. Jawaid, M. Thariq, and N. Saba, "Numerical modeling of hybrid composite materials," in *Modelling of Damage Processes in Biocomposites, Fibre-Reinforced Composites*, Cambridge: Woodhead Publishing, pp. 86–87.

[10] Y. Swolfs, L. Gorbatikh, and I. Verpoest, "Fibre hybridisation in polymer composites: A review," *Compos. Part A Appl. Sci. Manuf.*, vol. 67, pp. 181–200, 2014.

[11] G. Marsh, "Airbus A350 XWB update," *Reinf. Plast.*, vol. 54, no. 6, pp. 20–24, 2010.

[12] P. Beardmore and C. F. Johnson, "The potential for composites in structural automotive applications," *Compos. Sci. Technol.*, vol. 26, no. 4, pp. 251–281, 1986.

[13] U.S. Congress Office of Technology Assessment, "New Structural Materials Technologies: Opportunities for the Use of Advanced Ceramics and Composites-A Technical Memorandum, OTA-TM-E-32." U.S. Government Printing Office,

Washington, DC, pp. 50–53, 1986.

[14] M. Maria, “Advanced composite materials of the future in aerospace industry,” *Incas Bull.*, vol. 5, pp. 139–150, Sep. 2013.

[15] L. J. Korb, “Space Vehicles,” in *Engineering Applications of Composites: Composite Materials, Volume 3*, B. R. Noton, Ed. London: Academic Press, Inc. (London) Ltd., 1974, pp. 69–118.

[16] Y. Zhou, L. Yang, and Y. Huang, “Mechanical Properties of Composite Materials,” in *Micro- and Macromechanical Properties of Materials*, CRC Press, 2014, pp. 559–560.

[17] K. Kumar and D. Paulo, Eds., “Industrial Applications of Polymer Composite Materials,” in *Composites and Advanced Materials for Industrial Applications*, USA: IGI Global, 2018, pp. 10–11.

[18] P. K. Bajpai and I. Singh, Eds., “Fabrication of Composite Laminates,” in *Reinforced Polymer Composites: Processing, Characterization and Post Life Cycle Assessment*, Weinheim, Germany: Wiley-VCH Verlag GmbH & Co. KGaA, pp. 39–49.

[19] K. K. Chawla, “Composite materials : Science and Engineering,” Springer, 1998, pp. 134–141.

[20] S. Gholizadeh, “A review of non-destructive testing methods of composite materials,” in *Structural Integrity Procedia*, 2016, pp. 50–57.

[21] M. Tekieli, S. De Santis, G. de Felice, A. Kwiecień, and F. Roscini, “Application of Digital Image Correlation to composite reinforcements testing,” *Compos. Struct.*, vol. 160, pp. 670–688, 2017.

[22] P. Feres Filho, “Acoustic Emission Testing in Composite Materials,” in *Non-destructive Testing ’92*, C. Hallai and P. Kulcsar, Eds. Oxford: Elsevier, 1992, pp. 40–44.

[23] J. N. Reddy and A. Miravete, “Introduction and Preliminaries,” in *Practical Analysis of Composite Laminates*, Florida, USA: CRC Press, Inc., 1995, pp. 1–2.

[24] F. C. Campbell, “Liquid Molding,” in *Manufacturing Processes for Advanced Composites*, Oxford, UK: Elsevier B.V., 2004, pp. 331–349.

[25] S. V. Hoa, “Techniques for Composites Manufacturing,” in *Principles of the Manufacturing of Composite Materials*, USA: DEStech Publications, Inc., 2009, pp. 141–247.

[26] J. R. Fekete and J. N. Hall, “Design of auto body: Materials perspective,” in *Automotive Steels*, Woodhead Publishing, 2017, pp. 1–18.

[27] H. Nakatani, T. Yamada, Y. Nekoshima, and S. Ogihara, “Evaluation of Thin Titatnium

Films-CFRP Fiber Metal Laminates for Composite Bolted Joints," in *Design, Manufacturing and Applications of Composites: Proceedings of the Ninth Joint Canada-Japan Workshop on Composites*, 2012, pp. 7–13.

[28] R. K. Prusty, D. K. Rathore, B. P. Singh, S. C. Mohanty, K. K. Mahato, and B. C. Ray, "Experimental optimization of flexural behaviour through inter-ply fibre hybridization in FRP composite," *Constr. Build. Mater.*, vol. 118, pp. 327–336, 2016.

[29] A. R. Bunsell and B. Harris, "Hybrid carbon and glass fibre composites," *Composites*, vol. 5, no. 4, pp. 157–164, Jul. 1974.

[30] D. Chen, G. Sun, M. Meng, X. Jin, and Q. Li, "Flexural performance and cost efficiency of carbon/basalt/glass hybrid FRP composite laminates," *Thin-Walled Struct.*, vol. 142, pp. 516–531, 2019.

[31] J. Zhang, K. Chaisombat, S. He, and C. H. Wang, "Hybrid composite laminates reinforced with glass/carbon woven fabrics for lightweight load bearing structures," *Mater. Des.*, vol. 36, pp. 75–80, 2012.

[32] J. H. Song, "Pairing effect and tensile properties of laminated high-performance hybrid composites prepared using carbon/glass and carbon/aramid fibers," *Compos. Part B Eng.*, vol. 79, no. C, pp. 61–66, 2015.

[33] D. K. Jesthi and R. K. Nayak, "Improvement of mechanical properties of hybrid composites through interply rearrangement of glass and carbon woven fabrics for marine application," *Compos. Part B Eng.*, vol. 168, pp. 467–475, 2019.

[34] I. E. Tabrizi, A. Kefal, J. S. M. Zanjani, C. Akalin, and M. Yildiz, "Experimental and numerical investigation on fracture behavior of glass/carbon fiber hybrid composites using acoustic emission method and refined zigzag theory," *Compos. Struct.*, vol. 223, p. 110971, 2019.

[35] W. Zhou, H.-F. Yin, Y.-J. Shang, and P.-F. Zhang, "Failure behavior and damage visualization of thick carbon/aramid hybrid woven composites under flexural loading conditions," *Nondestruct. Test. Eval.*, pp. 1–19, Sep. 2019.

[36] Sudarisman, B. Miguel, and I. Davies, *The effect of partial substitution of E-glass fibre for carbon fibre on the mechanical properties of CFRP composites*. 2009.

[37] I. L. Kalnin, "Evaluation of Unidirectional Glass-Graphite Fiber/Epoxy Resin Composites," in *Composite Materials: Testing and Design (Second Conference)*, H. T. Corten, Ed. West Conshohocken, PA: ASTM International, 1972, pp. 551–563.

[38] N. L. Hancox and H. Wells, "Izod impact properties of carbon-fibre/glass-fibre sandwich

structures," *Composites*, vol. 4, no. 1, pp. 26–30, 1973.

[39] S. C. Khatri and M. J. Koczak, "Thick-section AS4-graphite/E-glass/PPS hybrid composites: Part II. Flexural response," *Compos. Sci. Technol.*, vol. 56, no. 4, pp. 473–482, 1996.

[40] P. W. Sonparote and S. C. Lakkad, "Mechanical properties of carbon/glass fibre reinforced hybrids," *Fibre Sci. Technol.*, vol. 16, no. 4, pp. 309–312, 1982.

[41] C. Dong and I. J. Davies, "Flexural and tensile moduli of unidirectional hybrid epoxy composites reinforced by S-2 glass and T700S carbon fibres," *Mater. Des.*, vol. 54, pp. 893–899, 2014.

[42] M. G. R. Sause, S. Schmitt, and S. Kalafat, "Failure load prediction for fiber-reinforced composites based on acoustic emission," *Compos. Sci. Technol.*, vol. 164, pp. 24–33, 2018.

[43] S. S. Kumar, N. V Londe, A. S. Saviraj, and V. Kannanth, "Effect of Accelerated Ageing on Hardness and Flexural Behaviour of Woven fabric Glass/ Carbon Hybrid Epoxy Composites," *Mater. Today Proc.*, vol. 4, no. 10, pp. 10751–10756, 2017.

[44] C. Dong, "Uncertainties in flexural strength of carbon/glass fibre reinforced hybrid epoxy composites," *Compos. Part B Eng.*, vol. 98, pp. 176–181, Aug. 2016.

[45] N. Beheshtizadeh, A. Mostafapour, and H. Abbasi, "Effect of fiber layout on signal analyzing of carbon/glass/epoxy hybrid composite laminates flexural loading using acoustic emission," *Measurement*, vol. 136, pp. 608–614, 2019.

[46] C. Dong and I. J. Davies, "Flexural and tensile strengths of unidirectional hybrid epoxy composites reinforced by S-2 glass and T700S carbon fibres," *Mater. Des.*, vol. 54, pp. 955–966, 2014.

[47] F. Mesquita, A. van Gysel, M. Selezneva, Y. Swolfs, S. V. Lomov, and L. Gorbatikh, "Flexural behaviour of corrugated panels of self-reinforced polypropylene hybridised with carbon fibre: An experimental and modelling study," *Compos. Part B Eng.*, vol. 153, pp. 437–444, Nov. 2018.

[48] C. Yilmaz *et al.*, "A hybrid damage assessment for E-and S-glass reinforced laminated composite structures under in-plane shear loading," *Compos. Struct.*, vol. 186, pp. 347–354, Feb. 2018.

[49] W. L. Cheng, S. Langlie, and S. Itoh, "High velocity impact of thick composites," in *International Journal of Impact Engineering*, 2003, vol. 29, no. 1–10, pp. 167–184.

[50] L. J. Deka, S. D. Bartus, and U. K. Vaidya, "Multi-site impact response of S2-

glass/epoxy composite laminates," *Compos. Sci. Technol.*, vol. 69, no. 6, pp. 725–735, May 2009.

[51] N. K. Naik and A. V. Doshi, "Ballistic impact behaviour of thick composites: Parametric studies," *Compos. Struct.*, vol. 82, no. 3, pp. 447–464, Feb. 2008.

[52] S. E. Boyd, T. A. Bogetti, J. M. Staniszewski, B. D. Lawrence, and M. S. Walter, "Enhanced delamination resistance of thick-section glass-epoxy composite laminates using compliant thermoplastic polyurethane interlayers," *Compos. Struct.*, vol. 189, pp. 184–191, 2018.

[53] J. Lee and C. Soutis, "A study on the compressive strength of thick carbon fibre-epoxy laminates," *Compos. Sci. Technol.*, vol. 67, no. 10, pp. 2015–2026, Aug. 2007.

[54] A. Djabali, L. Toubal, R. Zitoune, and S. Rechak, "Fatigue damage evolution in thick composite laminates: Combination of X-ray tomography, acoustic emission and digital image correlation," *Compos. Sci. Technol.*, vol. 183, p. 107815, Oct. 2019.

[55] D. Kim and R. A. Chaudhuri, "Effect of lamination sequence on the localization and shear crippling instability in thick imperfect cross-ply rings under external pressure," *Compos. Struct.*, vol. 80, no. 4, pp. 504–513, 2007.

[56] L. Iurlaro, M. Gherlone, M. Di Sciuva, and A. Tessler, "Refined Zigzag Theory for laminated composite and sandwich plates derived from Reissner's Mixed Variational Theorem," *Compos. Struct.*, vol. 133, pp. 809–817, 2015.

[57] A. Tessler, M. Di Sciuva, and M. Gherlone, "A Refined Zigzag Beam Theory for Composite and Sandwich Beams," *J. Compos. Mater.*, vol. 43, no. 9, pp. 1051–1081, Jan. 2009.

[58] A. Tessler, M. Di Sciuva, and M. Gherlone, "A consistent refinement of first-order shear deformation theory for laminated composite and sandwich plates using improved zigzag kinematics," *J. Mech. Mater. Struct.*, vol. 5, pp. 341–367, Aug. 2010.

[59] "ASTM D3039 / D3039M-17, Standard Test Method for Tensile Properties of Polymer Matrix Composite Materials." ASTM International, West Conshohocken, PA, 2017.

[60] "ASTM D5379 / D5379M-12, Standard Test Method for Shear Properties of Composite Materials by the V-Notched Beam Method." ASTM International, West Conshohocken, PA, 2017.

[61] "ASTM D790-17, Standard Test Methods for Flexural Properties of Unreinforced and Reinforced Plastics and Electrical Insulating Materials." ASTM International, West Conshohocken, PA, 2017.

[62] D. Hull and T. W. Clyne, *An Introduction to Composite Materials*, 2nd ed. Cambridge, UK: Cambridge University Press, 1996.

[63] K. Lee and S. W. Lee, "6 - Response of composite panels to blast wave pressure loadings," in *Woodhead Publishing Series in Civil and Structural Engineering*, N. B. T.-B. P. of C. I. and V. U. C. Uddin, Ed. Woodhead Publishing, 2010, pp. 212–232.

[64] B. Mohammadi and D. Salimi-Majd, "Investigation of delamination and damage due to free edge effects in composite laminates using cohesive interface elements," *Eng. Solid Mech.*, vol. 2, pp. 101–118, 2015.

[65] V. Chellappa and B. Z. Jang, "Crack growth and fracture behavior of fabric reinforced polymer composites," *Polym. Compos.*, vol. 17, no. 3, pp. 443–450, Jun. 1996.

[66] A. Amaro, P. Reis, and M. De Moura, "Delamination Effect on Bending Behaviour in Carbon–Epoxy Composites," *Strain*, vol. 47, pp. 203–208, Dec. 2008.